The ALMA-QUARKS Survey. III. Clump-to-core Fragmentation and Searches for High-mass Starless Cores

Dongting Yang, Hong-Li Liu, Tie Liu, Xunchuan Liu, Fengwei Xu, Sheng-Li Qin, Anandmayee Tej, Guido Garay, Xiaofeng Mai, Wenyu Jiao, et al.

The Astrophysical Journal Supplement Series, 280:33 (23pp), 2025 September https://doi.org/10.3847/1538-4365/adf847

The ALMA-QUARKS Survey. III. Clump-to-core Fragmentation and Searches for High-mass Starless Cores

Dongting Yang[1,41], Hong-Li Liu[1,41], Tie Liu[2], Xunchuan Liu[2], Fengwei Xu[3,4], Sheng-Li Qin[1], Anandmayee Tej[5], Guido Garay[6,7], Lei Zhu[7], Xiaofeng Mai[2,8], Wenyu Jiao[2], Siju Zhang[6], Sami Dib[9], Amelia M. Stutz[10], Aina Palau[11], Patricio Sanhueza[12], Annie Zavagno[13,14], A. Y. Yang[15,16], Xindi Tang[17], Mengyao Tang[18], Yichen Zhang[19], Pablo García[7,20], Tianwei Zhang[21], Anindya Saha[5], Shanghuo Li[22,23], Paul F. Goldsmith[24], Leonardo Bronfman[6], Chang Won Lee[25,26], Kotomi Taniguchi[27], Swagat Ranjan Das[6], Prasanta Gorai[28,29], Ariful Hoque[30], Li Chen[1], Zhiping Kou[1,17], Jianjun Zhou[17], Yankun Zhang[2], L. Viktor Tóth[31,32], Tapas Baug[30], Xianjin Shen[33,34], Chuanshou Li[1], Jiahang Zou[1,2], Ankan Das[35], Hafiz Nazeer[5], L. K. Dewangan[36], Jihye Hwang[37,38], and James O. Chibueze[39,40]

[1] School of Physics and Astronomy, Yunnan University, Kunming, 650091, People's Republic of China; dongting@mail.ynu.edu.cn, hongliliu2012@gmail.com
[2] Shanghai Astronomical Observatory, Chinese Academy of Sciences, 80 Nandan Road, Shanghai 200030, People's Republic of China; liutie@shao.ac.cn, liuxunchuan001@gmail.com
[3] Kavli Institute for Astronomy and Astrophysics, Peking University, 5 Yiheyuan Road, Haidian District, Beijing 100871, People's Republic of China; fengwei.astro@pku.edu.cn
[4] Department of Astronomy, Peking University, Beijing 100871, People's Republic of China
[5] Indian Institute of Space Science and Technology, Thiruvananthapuram 695 547, Kerala, India
[6] Departamento de Astronomía, Universidad de Chile, Casilla 36-D, Santiago, Chile
[7] Chinese Academy of Sciences South America Center for Astronomy, National Astronomical Observatories, Chinese Academy of Sciences, Beijing, 100101, People's Republic of China
[8] School of Astronomy and Space Sciences, University of Chinese Academy of Sciences, No. 19A Yuquan Road, Beijing 100049, People's Republic of China
[9] Max Planck Institute for Astronomy, Königstuhl 17, D-69117 Heidelberg, Germany
[10] Departamento de Astronomía, Universidad de Concepción, Casilla 160-C, Concepción, Chile
[11] Instituto de Radioastronomía y Astrofísica, Universidad Nacional Autónoma de México, Antigua Carretera a Pátzcuaro 8701, Ex-Hda. San José de la Huerta, Morelia, 58089, Michoacán, Mexico
[12] Department of Astronomy, School of Science, The University of Tokyo, 7-3-1 Hongo, Bunkyo, Tokyo 113-0033, Japan
[13] Aix-Marseille Univ, CNRS, CNES, LAM, 38 rue F. Joliot-Curie, 13013, Marseille, France
[14] Institut Universitaire de France, Paris, France
[15] National Astronomical Observatories, Chinese Academy of Sciences, Beijing, 100101, People's Republic of China
[16] Key Laboratory of Radio Astronomy and Technology, Chinese Academy of Sciences, A20 Datun Road, Chaoyang District, Beijing, 100101, People's Republic of China
[17] Xinjiang Astronomical Observatory, Chinese Academy of Sciences, 150 Science 1-Street, Urumqi, Xinjiang 830011, People's Republic of China
[18] Institute of Astrophysics, School of Physics and Electronic Science, Chuxiong Normal University, Chuxiong 675000, People's Republic of China
[19] Department of Astronomy, Shanghai Jiao Tong University, 800 Dongchuan Road, Minhang, Shanghai 200240, People's Republic of China
[20] Instituto de Astronomía, Universidad Católica del Norte, Av. Angamos 0610, Antofagasta, Chile
[21] Research Center for Astronomical computing, Zhejiang Laboratory, Hangzhou, People's Republic of China
[22] School of Astronomy and Space Science, Nanjing University, 163 Xianlin Avenue, Nanjing 210023, People's Republic of China
[23] Key Laboratory of Modern Astronomy and Astrophysics (Nanjing University), Ministry of Education, Nanjing 210023, People's Republic of China
[24] Jet Propulsion Laboratory, California Institute of Technology, 4800 Oak Grove Drive, Pasadena, CA 91109, USA
[25] Korea Astronomy and Space Science Institute, 776 Daedeokdae-ro, Yuseong-gu, Daejeon 34055, Republic of Korea
[26] University of Science and Technology, Korea (UST), 217 Gajeong-ro, Yuseong-gu, Daejeon 34113, Republic of Korea
[27] National Astronomical Observatory of Japan, National Institutes of Natural Sciences, 2-21-1 Osawa, Mitaka, Tokyo 181-8588, Japan
[28] Rosseland Centre for Solar Physics, University of Oslo, PO Box 1029 Blindern, 0315 Oslo, Norway
[29] Institute of Theoretical Astrophysics, University of Oslo, PO Box 1029 Blindern, 0315 Oslo, Norway
[30] S. N. Bose National Centre for Basic Sciences, Block-JD, Sector-III, Salt Lake City, Kolkata 700106, India
[31] Institute of Physics and Astronomy, Eötvös Loránd University, Pázmány Péter sétány 1/A, H-1117 Budapest, Hungary
[32] Faculty of Science and Technology, University of Debrecen, H-4032 Debrecen, Hungary
[33] Purple Mountain Observatory, Chinese Academy of Sciences, Nanjing 210008, People's Republic of China
[34] School of Astronomy and Space Science, University of Science and Technology of China, Hefei 230026, People's Republic of China
[35] Institute of Astronomy Space and Earth Science P 177, CIT Road, Scheme 7m, Kolkata 700054, India
[36] Astronomy & Astrophysics Division, Physical Research Laboratory, Navrangpura, Ahmedabad 380009, India
[37] Institute for Advanced Study, Kyushu University, Japan
[38] Department of Earth and Planetary Sciences, Faculty of Science, Kyushu University, Nishi-ku, Fukuoka 819-0395, Japan
[39] Department of Mathematical Sciences, University of South Africa, Cnr Christian de Wet Road and Pioneer Avenue, Florida Park, 1709, Roodepoort, South Africa
[40] Department of Physics and Astronomy, Faculty of Physical Sciences, University of Nigeria, Carver Building, 1 University Road, Nsukka 410001, Nigeria
Received 2025 May 31; revised 2025 July 21; accepted 2025 August 4; published 2025 September 3

Abstract

The Querying Underlying mechanisms of massive star formation with ALMA-Resolved gas Kinematics and Structures (QUARKS) survey observed 139 infrared-bright (IR-bright) massive protoclusters at 1.3 mm

[41] Both authors contributed equally to this work.

wavelength with the Atacama Large Millimeter/submillimeter Array (ALMA). This study investigates clump-to-core fragmentation and searches for candidate high-mass starless cores within IR-bright clumps using combined ALMA 12 m (C-2) and Atacama Compact Array 7 m data, providing $\sim$1″ ($\sim$0.02 pc at 3.7 kpc) resolution and $\sim$0.6 mJy beam^{-1} continuum sensitivity ($\sim$0.3 $M_{\odot}$ at 30 K). We identified 1562 compact cores from 1.3 mm continuum emission using *getsf*. Observed linear core separations ($\lambda_{\rm obs}$) are significantly less than the thermal Jeans length ($\lambda_{\rm J}$), with the $\lambda_{\rm obs}/\lambda_{\rm J}$ ratios peaking at $\sim$0.2. This indicates that thermal Jeans fragmentation has taken place within the IR-bright protocluster clumps studied here. The observed low ratio of $\lambda_{\rm obs}/\lambda_{\rm J} \ll 1$ could be the result of evolving core separation or hierarchical fragmentation. Based on associated signatures of star formation (e.g., outflows and ionized gas), we classified cores into three categories: 127 starless, 971 warm, and 464 evolved cores. Two starless cores have masses exceeding 16 $M_{\odot}$, and represent high-mass candidates. The scarcity of such candidates suggests that competitive accretion-type models could be more applicable than turbulent core accretion-type models in high-mass star formation within these IR-bright protocluster clumps.

Unified Astronomy Thesaurus concepts: Interstellar medium (847); Dust continuum emission (412); Submillimeter astronomy (1647); Molecular clouds (1072); Star forming regions (1565); Protoclusters (1297); Massive stars (732); Protostars (1302)

Materials only available in the online version of record: machine-readable tables

1. Introduction

High-mass stars ($>8\,M_{\odot}$) play a key role in the Universe as primary sources of ionizing radiation, heavy element production, interstellar medium mixing and turbulence, and as important ingredients of galactic structure and evolution (e.g., S. Dib et al. 2006; H. Zinnecker & H. W. Yorke 2007; C. L. Dobbs et al. 2014). The formation mechanism of high-mass stars has long been a central topic in astrophysics (F. Motte et al. 2018).

The transition from a clump to cores represents a critical stage in high-mass star formation (e.g., H. Beuther et al. 2025). Two mainstream theoretical models—the "turbulent core accretion" model (C. F. McKee & J. C. Tan 2003) and the "competitive accretion" model (I. A. Bonnell et al. 2001)—describe this transition invoking different physical processes. In the turbulent core accretion model, a (few) prestellar core(s) are preassembled within a massive clump and supported by strong turbulence and/or magnetic fields. The fast gas accretion from the gas reservoir within the clump during the monolithic-like collapse process determines the final mass of a (few) high-mass star(s). While in the competitive accretion model, low-mass cores first form from thermal Jeans fragmentation of massive clumps and contiune accreting from beyond their immediate environment, for example through large-scale filamentary accretion flows (E. Vázquez-Semadeni et al. 2019; P. Padoan et al. 2020). Such a multiscale dynamical mass accretion scenario facilitates the formation of high-mass stars (e.g., N. Peretto et al. 2013; H.-L. Liu et al. 2022a; L. K. Dewangan et al. 2023; D. Yang et al. 2023; A.-X. Luo et al. 2024a, 2024b; S. Pan et al. 2024).

The validation of both models requires high-resolution and sensitive (sub)millimeter observations to spatially resolve individual dense cores. Recent (sub)arcsecond observations appear to overwhelmingly support the competitive accretion scenario. For instance, fragmentation of massive clumps into clusters of low-mass cores has been commonly observed (e.g., P. Sanhueza et al. 2019; B. E. Svoboda et al. 2019; A. Coletta et al. 2025). In contrast, high-mass prestellar cores—defined as those having $>16M_{\odot}$ within 0.01–0.1 pc and considered as key evidence for the turbulent core accretion model—are rarely detected and are mostly limited to case studies if any (K. Wang et al. 2014; A. Palau et al. 2015; T. Liu et al. 2017; A. T. Barnes et al. 2023; T. Nony et al. 2023; X. Mai et al. 2024; M. Valeille-Manet et al. 2025). This low detection rate implies a very short lifetime for high-mass prestellar cores (F. Motte et al. 2018).

Previous searches for high-mass prestellar cores have been dedicated to focusing primarily on infrared dark (IR-dark) clouds (IRDCs; e.g., G11.11-P6-SMA1 reported in K. Wang et al. 2014; "dragon cloud"-C2c1a in A. T. Barnes et al. 2023; G34-MM1-E1 in X. Mai et al. 2024), which are considered to be at the earliest stages of high-mass star formation. However, star formation within a massive clump is not necessarily synchronous; in fact, there may be an age sequence, allowing high-mass prestellar cores to exist even in more evolved clumps where other stars have already begun forming. Recent ALMA statistical studies have shown that dense core masses grow significantly from IRDCs to more evolved IR-bright protostellar clumps (H.-L. Liu et al. 2023; F. Xu et al. 2024a). This suggests that evolved clumps could harbor more massive starless cores. This finding motivates searches for high-mass starless cores not only in IRDCs but also in more evolved IR-bright environments. In a sample of 11 IR-bright massive clumps, F. Xu et al. (2024a) found that the maximum starless core mass could be up to 18.4 $M_{\odot}$, twice that revealed in IRDCs by P. Sanhueza et al. (2019). M. Valeille-Manet et al. (2025) analyzed the ALMA-IMF data $\sim$2000 au resolution toward 15 high-mass star-forming regions, reporting 12 candidate high-mass prestellar cores ($>16\,M_{\odot}$). Such efforts could therefore provide critical observational constraints on the turbulent core accretion model, testing whether the low detection rate of high-mass starless cores is due to previous observational biases or to their intrinsic rarity.

The physical drivers of clump fragmentation remain debated, with turbulence and thermal pressure being the primary contenders. Some studies argued for the dominance of turbulence, which was thought to increase the Jeans mass and Jeans length, as observed in several IRDCs (Q. Zhang et al. 2009; T. Pillai et al. 2011; P. Sanhueza et al. 2013; K. Wang et al. 2014; S. Li et al. 2019; W. Jiao et al. 2023; A. Avison et al. 2023). Conversely, high-angular-resolution observations toward other massive clumps with varying evolutionary stages, including IR-dark and IR-bright environments, align with a thermal fragmentation scenario (A. Palau et al. 2015; H. Beuther et al. 2018; B. E. Svoboda et al. 2019; P. Sanhueza et al. 2019; X. Lu et al. 2020; A. Saha et al. 2022; M. Tang et al. 2022; K. Ishihara et al. 2024; K. Morii et al. 2024). Additionally, F. Xu et al. (2024a) reported that most observed core separations within

evolved IR-bright clumps are significantly less than the predicted thermal Jeans length. This was attributed to a decrease of core separation over time due to persistent global gravitational collapse during evolution (I. A. Bonnell et al. 2001; H. Beuther et al. 2018; A. Traficante et al. 2023). Other factors, such as magnetic fields and initial density profiles within massive clumps, have also been explored in the literature, where strong magnetic fields and a concentrated density profile were assumed to effectively reduce fragmentation and thus lead to the formation of more massive cores for high-mass star formation (P. Girichidis et al. 2011; B. Commerçon et al. 2011; T. Peters et al. 2011; A. Palau et al. 2014; F. Fontani et al. 2016; A. Palau et al. 2021; P. Hennebelle et al. 2022; P. Sanhueza et al. 2025).

Thanks to ALMA's high angular resolution and sensitivity, the ALMA Three-millimeter Observations of Massive Star-forming regions (ATOMS; T. Liu et al. 2020) survey has observed a sample of 146 massive IR-bright protocluster clumps in band 3 (∼3 mm). The sample was selected based on their bright CS ($J = 2 - 1$) emission ($T_b > 2$ K) from a homogeneous Galactic plane survey of candidate ultracompact H II (UCHII) regions (L. Bronfman et al. 1996). The ATOMS survey was aimed to address several key objectives, including but not limited to (1) establishing a high-angular-resolution catalog of high-mass star formation dense cores (T. Liu et al. 2020; H.-L. Liu et al. 2021); (2) investigating the chemistry of hot molecular cores (HMCs; S.-L. Qin et al. 2022; Y. Peng et al. 2022; L. Chen et al. 2025; Z. Kou et al. 2025; Z.-Y. Li et al. 2025); (3) studying UCHII regions (e.g., physical properties and associated feedback mechanisms (T. Liu et al. 2020; H.-L. Liu et al. 2021; J.-W. Zhou et al. 2021; C. Zhang et al. 2022, 2023a; S. Zhang et al. 2023b); and (4) characterizing prevailing filamentary structures, and their kinematics and dynamics (J.-W. Zhou et al. 2021; H.-L. Liu et al. 2022a; R. Liu et al. 2022b; J.-W. Zhou et al. 2022; A. Saha et al. 2022; F.-W. Xu et al. 2023; D. Yang et al. 2023; S. R. Das et al. 2024).

As a follow-up to the ATOMS program, and for advancing the scientific objectives already established therein, the Querying Underlying mechanisms of massive star formation with ALMA-Resolved gas Kinematics and Structures (QUARKS; see Section 2 for details on observations) survey was designed with high-angular-resolution capabilities in ALMA band 6 (∼1.3 mm). This study focuses on clump-to-core fragmentation and searches for candidate high-mass starless cores within IR-bright clumps using combined ALMA 12 m compact array C-2 (TM2) and Atacama Compact Array (ACA) 7 m data of the QUARKS survey. This paper is organized as follows: Section 2 describes the ALMA observations and data reduction for the QUARKS survey. Section 3 presents the analysis of the TM2+ACA combined data, including the core extraction procedure (Section 3.1), dense core classification (Section 3.2), physical parameter estimation (Section 3.3), analysis of core separation (Section 3.4) and thermal Jeans length analysis within protocluster clumps (Section 3.5). Section 4 discusses fragmentation of IR-bright massive protocluster clumps and search results of candidate high-mass starless cores. Section 5 summarizes the major results.

2. ALMA Observations and Data Reduction

2.1. QUARKS Sample and ALMA Observations

The QUARKS survey (PIs: Lei Zhu, Guido Garay, and Tie Liu; Project ID: 2021.1.00095.S; X. Liu et al. 2024) is a follow-up program to the ATOMS survey, offering a higher angular resolution (QUARKS ∼0.″3 for the best angular resolution versus ATOMS ∼2″) in ALMA band 6. After ruling out seven protocluster clumps not having enough detectable 3mm continuum emission in the ATOMS survey, in the QUARKS survey we observed 139 IR-bright massive protocluster clumps (X. Liu et al. 2024; F. Xu et al. 2024b).

Due to the difference in frequency setup between the two surveys, the field of view (FoV) of the QUARKS only covers a portion of that by the ATOMS (i.e., for the ALMA 12 m array, FoV ∼ 20″ in band 6 for QUARKS versus FoV ∼ 40″ in band 3 for ATOMS). Thus, the QUARKS observations were optimized to cover the densest part of the 139 IR-bright protocluster clumps. To observe extended filamentary structures in 17 of 139 protocluster clumps (e.g., I08448-4343; D. Yang et al. 2024), two pointing observations were allocated for each of them. Therefore, the QUARKS survey consists of a total of 156 single pointings (e.g., fields) to observe 139 protocluster clumps. In addition, for each field, the QUARKS observations were obtained with three different ALMA configurations. That is, relatively low (∼5″), moderate (∼1″), and high (∼0.″3) angular resolution observations were conducted by the ACA 7 m array, ALMA 12 m compact array C-2 (TM2) and extended C-5 (TM1) configurations, respectively (see Table 1 in X. Liu et al. 2024). ACA observations were first completed in late 2022 May (F. Xu et al. 2024b), followed by TM2 and TM1 that proceeded until 2024 June.

Based on similar sky coordinates, the QUARKS 156 fields were grouped into 15 scheduling blocks, which are referred to as "Group." For TM2 observations, the Group ID, number of fields, and source name within each Group are listed in columns (1)–(3) of Table 1. Note that the Groups are sorted in ascending order by source name. The date of TM2 observations is listed in column (4) of Table 1, starting on 2022 April 9, and completed on 2024 March 22. Note that two execution blocks were performed on different observing dates for Group 5 and Group 15. In the QUARKS TM2 observations, except for Group 1, all Groups have similar minimum and maximum baselines (BL; ∼15.1–313.7 m), angular resolution (AR; ∼1″), and maximum recoverable scale (MRS; ∼11″), which are listed in columns (5)–(7) of Table 1. The phase and bandpass calibrators are listed in columns (8) and (9) of Table 1, respectively.

The ALMA band 6 receivers were used in a dual-polarization mode for the QUARKS observations. Four spectral windows (SPWs 1–4) were configured with a bandwidth of ∼2 GHz and a velocity resolution of ∼1.3 km s^{-1} for each SPW. The frequencies of the four SPWs were centered at approximately 217.92, 220.32, 231.37, and 233.52 GHz, respectively. The wide range of four SPWs cover numerous major molecular line transitions at ∼1.3 mm, including but not limited to (1) a cold-gas tracer (e.g., N_2D^+ 3–2); (2) outflow gas tracers (e.g., CO (2–1), SiO (5–4), H_2CO (3–2)); (3) HMC tracers (e.g., CH_3CN (12–11)), and (4) an ionized gas tracer, H30α. More information about the major molecular lines at 1.3 mm typical of different gas environments has been summarized in Table 2 of X. Liu et al. (2024).

2.2. Data Reduction

In this study, the ACA and TM2 observations of the QUARKS survey were combined and imaged using Common

Table 1
QUARKS TM2 Observations

Group ID[a]	N_{field}[b]	Source	Obs. Date	Min./Max. BL (m/m)	AR (arcsec)	MRS (arcsec)	Calibrators	
							Phase	Bandpass/Flux
(1)	(2)	(3)	(4)	(5)	(6)	(7)	(8)	(9)
1	7	08303-09094	2022-12-29	15.1/500.6	0.7	7.3	J0922-3959	J1037-2934
2	4	10365-11332	2024-03-19	15.1/313.7	1.1	11.1	J1047-6217	J1107-4449
3	15	12320-13295	2024-03-22	15.1/313.7	1.1	10.9	J1254-6111	J1427-4206
4	8	13471-14212	2024-03-18	15.1/313.7	1.1	10.9	J1408-5712	J1427-4206
5	5	14382-15290	2024-03-21	15.1/313.7	1.1	11.1	J1524-5903	J1427-4206
			2024-04-12	15.1/313.7	1.0	10.4	J1524-5903	J1427-4206
6	28	15384-16177	2024-03-22	15.1/313.7	1.0	10.9	J1603-4904	J1427-4206
7	19	16272-16489	2024-03-19	15.1/313.7	1.1	11.1	J1650-5044	J1617-5848
8	7	16524-17016	2024-03-19	15.1/313.7	1.1	11.1	J1711-3744	J1617-5848
9	15	17136-17278	2024-03-22	15.1/313.7	1.1	10.9	J1720-3552	J1617-5848
10	4	17439-17455	2022-04-09	15.1/313.7	1.1	9.5	J1744-3116	J1924-2914
11	6	17545-18075	2024-03-19	15.1/313.7	1.1	11.1	J1755-2232	J1924-2914
12	13	18079-18264	2024-03-19	15.1/313.7	1.1	11.1	J1832-2039	J1924-2914
13	11	18290-18341	2024-03-19	15.1/313.7	1.1	11.1	J1832-2039	J1924-2914
14	11	18411-18530	2022-10-26	14.8/312.7	1.1	9.8	J1851+0035	J1924-2914
15	3	19078-19097	2024-03-06	15.1/313.7	1.1	10.4	J1919-2914	J1924-2914
			2024-03-19	15.1/313.7	1.1	11.1	J1919-2914	J1924-2914

Notes.
[a] The QUARKS TM2 observations were arranged into 15 scheduling blocks, which are called "Groups" for short.
[b] The number of single-pointing fields conducted in each group.

Astronomy Software Applications (CASA, version 6.6.0, CASA Team et al. 2022) for both continuum and spectral line emission. Figure 1 presents an overview of the data reduction procedure. The *Auto-Flag* step was initially conducted to identify line-free channels and subsequently flag data. The *tclean* algorithm was then used to generate the first version of the combined TM2+ACA line data cubes for each field. To optimize the identification of the line-free channels, the *Manual-Flag* step was involved iteratively to produce the final continuum (with minimum contamination from line emission) and line data products. Details on data reduction are given below.

2.2.1. Data Flag and Basic Setup of Data Reduction

As shown in Figure 1, the raw visibility data for the QUARKS ACA and TM2 observations were first concatenated using the CASA task *concat*. In order to execute the CASA task *flag*, line-free channels need to be determined for each field. For this, we followed the method developed by X. Liu et al. (2024) for the QUARKS survey. Here, (1) molecular transitions of strong emission lines in the four SPWs were identified as a model spectrum by matching the ALMA pipeline-reduced data cube with the laboratory database of spectral lines (CDMS; H. S. P. Müller et al. 2001); (2) based on the centroid velocity (V_{lsr}) of each field, we shifted the model spectrum and expanded it to a width of 50 km s^{-1}, ensuring clean channels that are free of multiple velocity components and broad spectral line wing emission. The above approach yields line-free channels automatically. Line-emission channels were then flagged for continuum and line-free channels for four SPWs that were subtracted in the Fourier space employing the CASA task *uvcontsub* with a linear fitting (fitorder = 1). We refer to this process as the *Auto-Flag* step. The combined imaging processes of both continuum and lines were performed using the CASA task *tclean*, with a *briggs* robust weighting of 0.5. This constitutes the first version of the TM2+ACA data for both continuum and spectral lines (see Figure 1).

However, the TM2+ACA first version data reveal a skewed baseline for some fields instead of a constant level. This could be attributed to complex molecular spectral lines or more extended line wings, which resulted in contaminated line-free channels generated in the *Auto-Flag* step. Therefore, we manually reidentified the line-free channels for each field based on the TM2+ACA first version data using *Linemarker*.[42] Line-free channels were then flagged before the next continuum and line imaging. This is refered to as the *Manual-Flag* step (see Figure 1).

In the image-cleaning process, the image size for each field in Group 1 was set to be [300, 300] pixels, with a pixel size of 0.″15; for the fields in Groups 2–15 each image was set to have [250, 250] pixels, with a pixel size of 0.″2. The different settings mentioned above are due to the various angular resolutions between Group 1 and other groups (see Table 1). The image-cleaning procedure was conducted within a *pblimit* of 0.2 in each field.

In addition, as mentioned in Section 2.1, 17 protocluster clumps with extended density structures inside were covered by two single pointings. For 15 of them, we made the mosaic before imaging. However, the I12572-6316 and I17269-3312 protocluster clumps were excluded for the mosaic imaging because of the insufficient overlap between the two associated single pointings.

[42] https://gitee.com/liuxunchuan/linemarker; a tool for manually identifying the line-free or line-emission channels in an astronomical spectrum.

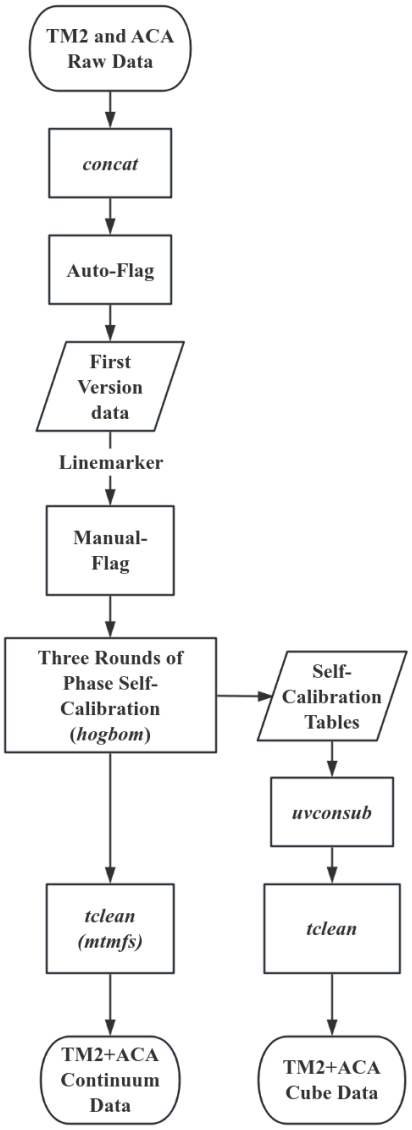

Figure 1. Flow chart for ALMA-QUARKS ACA and TM2 combined data reduction. The elliptical boxes denote the raw data and the final reduced data. The rectangle indicates a specific processing step, while the parallelogram indicates an intermediate product during the data reduction.

2.2.2. Continuum Imaging with Self-calibration

All four SPWs' visibility data were used to ensure a rather high sensitivity for the QUARKS TM2+ACA continuum image. In addition, the self-calibration approach was applied to improve the dynamic range of the reduced image by correcting the visibility phase/amplitude via the comparison of the visibility data with the model of the source itself (A. M. S. Richards et al. 2022). For continuum imaging, we performed three rounds of phase self-calibration (see Figure 1), each based on the *tclean* results of the previous round. Here, we selected the *hogbom* deconvolving algorithm, which uses a point-source model of the sky brightness distribution for operation, and is a better choice in the iterative phase self-calibration process. Subsequently, multiterm multi-frequency synthesis (*mtmfs*) with an *nterm* of 2 was employed for the last *tclean* procedure, which both restores the extended structure and improves the image quality (U. Rau & T. J. Cornwell 2011). Self-calibration was carried out manually and iteratively to optimize the cleaning thresholds, ensuring a rather good sensitivity while preventing divergence. As a result, the average noise level of the reduced TM2+ACA continuum data is $\sim$0.6 mJy beam^{-1}, with an average beam size of $\sim 1\farcs3 \times 1\farcs1$, corresponding to a mass sensitivity of $\sim 0.3\,M_{\odot}$ for a 30 K dust temperature at a median distance of 3.7 kpc for the QUARKS survey.

2.2.3. Line Imaging

For molecular lines, we applied to four SPWs to all the calibration tables from three rounds of continuum self-calibration (see Section 2.2.2), and subtracted emission of line-free channels in the Fourier space by employing the CASA task *uvcontsub* with a linear fitting (fitorder = 1) (see Figure 1). The subtracted TM2 and ACA visibility data were concatenated and subsequently cleaned to generate the spectral cube using the CASA task *tclean*, with the *mutilscale* deconvolution approach and a uniform cleaning threshold of 25 mJy beam^{-1} ($\sim$0.4 K). This threshold was chosen to optimize the cleaning performance of spectral cubes for most fields. As a result, the average rms level of the reduced line data is $\sim$10 mJy beam^{-1} ($\sim$0.2 K) per channel at an average synthesized beam of $\sim 1\farcs4 \times 1\farcs1$ and a velocity resolution of $\sim$1.3 km s^{-1}.

3. Results and Analysis

3.1. Core Extraction

Figure 2 presents a comparison of continuum images between the 3 mm ATOMS data (left panels) and the 1.3 mm QUARKS TM2+ACA data (right panels) for two example targets. The figure demonstrates the overall spatial consistency between 1.3 and 3 mm emission. The QUARKS images, owing to their higher angular resolution, reveal finer structures such as dense filaments and cores. In contrast, ATOMS 3 mm emission appears more extended, which results from the larger maximum recoverable scale of the ATOMS survey ($\sim$20″) and/or contribution from free–free emission at 3 mm. Free–free emission from ionized gas could radiate significantly at 3 mm, particularly within rather evolved clumps associated with UCHII regions, while at 1.3 mm, thermal dust emission could be the major component (e.g., A. Ginsburg et al. 2020; F. Motte et al. 2022). As shown in the right panels of Figure 2, the red contours correspond to emission of the H40α recombination line representative of ionized gas from the ATOMS survey, which does show a somehow extended emission morphology.

We employed the *getsf* algorithm (A. Men'shchikov 2021) to identify compact structures within the TM2+ACA continuum data at 1.3 mm. This algorithm has been widely used for extracting compact sources in complex protocluster environments (Y. Pouteau et al. 2022; T. Nony et al. 2023; L. K. Dewangan et al. 2024; F. Louvet et al. 2024; D. Yang et al. 2024; F. Xu et al. 2024a; 2025). In our case, the *getsf* was applied to images without primary beam correction, as they exhibit a relatively uniform noise level across the entire field of view. For the algorithm's configuration, we set the minimum and maximum sizes of the extracted compact sources to half and 3 times the synthesized beam size, respectively. Note that the choice of minimum size (whether half- or one-beam size) does not significantly influence the

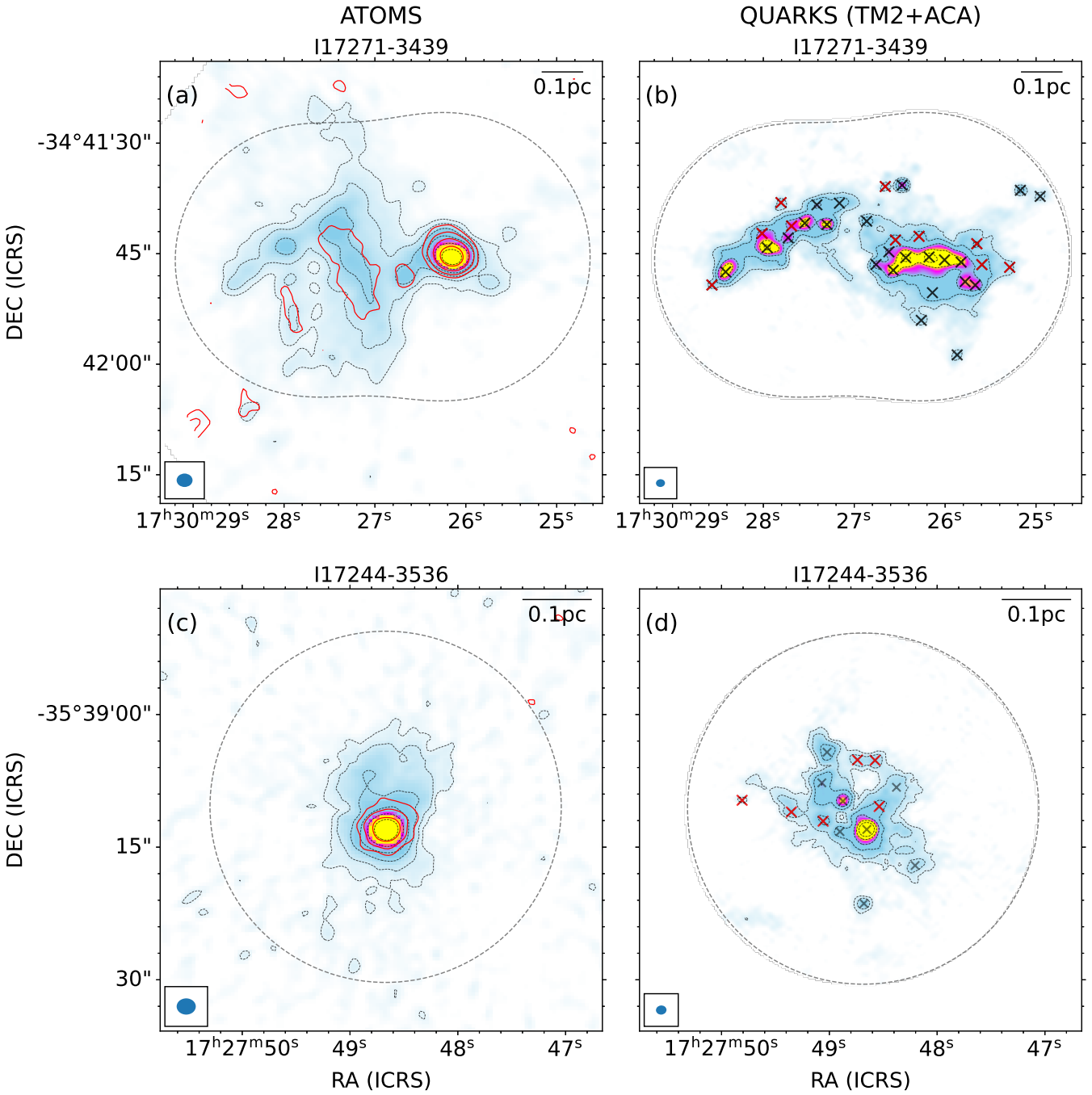

Figure 2. Comparison of ATOMS 3 mm and QUARKS 1.3 mm continuum images for two protocluster clumps. The black dashed circle in each panel defines the field of view of the QUARKS survey. Left panels ((a), (c)): ATOMS 3 mm continuum emission. The dashed contour levels are [3, 6, 12, 24, 48, 96] rms, with rms ∼1.4 and ∼0.4 mJy beam^{-1} for I17271-3439 and I17244-3536, respectively. Red contours correspond to integrated emission of the H40α recombination line representative of ionized gas from the ATOMS survey, with rms ∼0.2 and ∼0.1 Jy beam^{-1} km s^{-1} for I17271-3439 and I17244-3536, respectively. Right panels ((b), (d)): QUARKS TM2+ACA 1.3 mm continuum emission. The contour levels are the same as in the left panels, but with rms ∼2.1 and ∼0.4 mJy beam^{-1} for I17271-3439 and I17244-3536, respectively. The cross symbols correspond to the cores extracted from 1.3 mm continuum emission using the *getsf* algorithm, where black markers denote those detected by the algorithm at a configuration with a minimum source size employing the beam size, while red markers correspond to relatively faint cores detected at the other configuration employing half-beam. The beam sizes of ATOMS and QUARKS TM2+ACA continuum emission are shown on the lower left, and the 0.1 pc scale bar is on the upper right of each panel.

parameters (e.g., size, flux) of the extracted sources with strong emission, but the former parameter configuration can extract relatively weaker structures, which enables a sample of fragments as complete as possible for clump-to-core fragmentation analysis. As shown in the right panels of Figure 2, the red cross symbols represent the additional faint structures identified by the *getsf* using half of the beam size as the minimum size.

To enhance the reliability of our core sample, we applied a postselection process based on the quality-check parameters provided by the *getsf* algorithm. Specifically, we retained only the cores with a significance level (*SIGNM*; detection significance from monochromatic single scales) greater than 5 and a goodness (*GOODM*; monochromatic goodness combining significance and signal-to-noise ratio) greater than unity (M. Benedettini et al. 2018), while excluding the cores

Table 2
Core Parameters Measured by *getsf*

Source Name	Core	Dist. (kpc)	R.A. (IRCS) (h:m:s)	Decl. (IRCS) (d:m:s)	Maj. (arcsec)	Min. (arcsec)	PA (deg)	$F_{1.3mm}^{int}$ [a] (mJy)	$F_{1.3mm}^{peak}$ [a] (mJy beam^{-1})	*SIGNM*	*GOODM*
(1)	(2)	(3)	(4)	(5)	(6)	(7)	(8)	(9)	(10)	(11)	(12)
I08303-4303	1	2.35	$8^h32^m08^s.64$	$-43^d13^m45^s.65$	1.195	0.9643	27.43	134.16(1.48)	14.59(0.51)	171	705
I08303-4303	2	2.35	$8^h32^m09^s.05$	$-43^d13^m43^s.33$	0.9634	0.8254	93.93	33.38(1.08)	5.96(0.56)	74	116
I08303-4303	3	2.35	$8^h32^m08^s.46$	$-43^d13^m49^s.13$	1.453	1.039	38.52	52.66(1.4)	5.88(0.6)	59	82
I08303-4303	4	2.35	$8^h32^m08^s.46$	$-43^d13^m47^s.22$	1.081	1.029	0.6709	28.22(1.06)	4.17(0.62)	31	40
I08303-4303	5	2.35	$8^h32^m08^s.90$	$-43^d13^m52^s.12$	1.148	0.8792	11.07	6.17(0.38)	1.03(0.19)	12	8
I08303-4303	6	2.35	$8^h32^m08^s.88$	$-43^d13^m42^s.05$	2.086	1.466	99.41	7.55(0.91)	0.48(0.37)	13	3

Note.
[a] The values in parentheses represent the measurement errors.

(This table is available in its entirety in machine-readable form in the online article.)

Table 3
Criteria of Core Classification

Type of Cores	Criteria	Assumed Temperature
Candidate starless core	$N_{line} \leqslant 6$ without outflows and H30α emission	[20 K, T_{clump}][a]
Candidate warm core	$6 < N_{line} \leqslant 15$ without H30α emission	30 K
	Or $N_{line} \leqslant 6$ with outflows but no H30α emission	⋯
Evolved cores:	⋯	100 K
Candidate hot molecular core	$N_{line} > 15$ without H30α emission	⋯
Candidate UCHII-*h* core	With H30α emission and high line richness ($N_{line} > 15$)	⋯
Candidate UCHII-*l* core	With H30α emission and low line richness ($N_{line} \leqslant 15$)	⋯

Notes.
[a] T_{clump} is the average dust temperature of the natal clump.

located at the edges of each field. Cores with a value of *GOODM* below unity were considered highly unreliable (A. Men'shchikov 2021). The *SIGNM* and *GOODM* values for each core are listed in columns (11) and (12) of Table 2.

Following the above criteria, a total of 1562 compact structures (i.e., cores) were identified across 156 fields. The core parameters derived from *getsf*, with the integrated flux and peak intensity corrected for the primary beam response, are presented in Table 2. It is worth noting that although the majority of compact cores in each field can be identified by *getsf* using our criteria, a few potential sources could be still missing. As shown in Figure 2(d) for example, two or three relatively weak continuum peaks lack corresponding compact core identifications. This arises due to their low intensity contrast relative to background emission, and therefore those weak density structures could not be recognized by *getsf* (A. Men'shchikov 2021). Except for I13134-6242 and I18056-1952 (each with three dense cores), our clump sample contains 4 to 33 cores, which provides rather sufficient core numbers for our following fragmentation analysis.

3.2. Classification of Cores

We used molecular line emission from four SPWs in the QUARKS survey to classify the cores into distinct evolutionary stages of star formation. The four SPWs cover a wide frequency range of approximately 8 GHz, encompassing numerous molecular transitions that probe star-forming environments across various evolutionary stages, from starless cores to UCHII regions. The classification criteria are summarized in Table 3, with further details on each category of cores provided below. The number of detectable molecular lines (N_{line}) serves as a quantitative and efficient metric to assess the chemical complexity of the cores, enabling an approximate determination of their evolutionary stage (H.-L. Liu et al. 2021).

To determine N_{line} for each core, we identified the number of line-emission peaks from the core-averaged spectra exceeding a 3σ noise level across the four SPWs. The 1σ noise level was calculated as the standard deviation of the amplitudes in the line-free emission channels for each core ($\sim$20 mJy beam^{-1} on average). The resulting N_{line} values for each core are listed in column (6) of Tables 4 and 5. Note that N_{line} could be underestimated for cores having a large number of complex molecular transitions (e.g., $N_{line} > 50$), though this does not affect our major classification results.

Using N_{line} in conjunction with other star formation indicators (e.g., outflows and ionized gas), we categorized the 1562 identified cores into three primary groups: (1) candidate starless cores, (2) candidate warm cores (WCs), and (3) candidate evolved cores. The evolved core category was further subdivided into three subcategories based on H30α ionized gas emission: candidate HMCs, candidate UCHII region cores with a relatively high line richness ($N_{line} > 15$; UCHII-*h*), and candidate UCHII region cores with a relatively low line richness ($N_{line} \leqslant 15$; UCHII-*l*). Assuming that stronger ionized gas feedback occurring in later evolutionary

stages reduces the richness of molecular line emission (e.g., M. A. Requena-Torres et al. 2006; H. Beuther et al. 2008; S.-L. Qin et al. 2015), UCHII-*l* cores could be considered more evolved than UCHII-*h* ones.

3.2.1. Candidate Starless and Warm Cores

Candidate starless cores are defined here based on the two following criteria. First, they exhibit gas emission from some molecular transitions covered in the QUARKS survey with upper energy levels (E_u) below 22 K (P. Sanhueza et al. 2019). In accordance with this, six line transitions are considered relevant, namely CO/^{13}CO/C^{18}O (2–1) with $E_u \sim 16$ K, H_2CO ($3_{0,3}$–$2_{0,2}$) with $E_u = 20.96$ K, DCN (3–2) with $E_u = 20.85$ K, and N_2D^+ (3–2) with $E_u = 22.2$ K. Thus, candidate starless cores are required to only have such cold-gas emission of lines with $N_{\rm line} \leqslant 6$. Second, such candidates should lack any star formation signatures, such as outflows traced by CO emission or ionized gas by H30α emission (e.g., A. Y. Yang et al. 2018; P. Sanhueza et al. 2019; A. Y. Yang et al. 2022; J. S. Urquhart et al. 2022). Following the above standard, 127 (8.1%) out of 1562 cores were finally classified as candidate starless cores (see Figure 3). In addition, H_2CO ($3_{0,3}$–$2_{0,2}$) and DCN (3–2) line emission could trace low-velocity outflows (C. Codella et al. 2012). However, by examining the core-averaged spectra of these two lines for the 127 starless candidates, no broad-line wings were observed in the spectral line profiles (not shown here). This further suggests the starless possibility of these cores. Figure 4(a) presents typical molecular line spectra for a candidate starless core, which shows a few lines not signifying any star-forming signatures as mentioned earlier.

WCs are defined here to represent a transitional phase between starless and HMCs. In this study, molecular transitions with upper energy levels below ~100 K typical of hot-gas tracers but above ~22 K typical of cold-gas tracers, such as CH_3OH (4–3) with $E_u = 45.46$ K, H_2CO ($3_{2,2}$–$2_{2,1}$/$3_{2,1}$–$2_{2,0}$) with $E_u = 68.09$ K, SiO (5–4) with $E_u = 31.26$ K, SO (6–5) with $E_u = 34.98$ K, and ^{13}CS (5–4) with $E_u = 33.29$ K, are approximately designated as warm-gas tracers (e.g., P. Sanhueza et al. 2019). This rough definition allows us to estimate the number of emission lines for candidate WCs to be $6 < N_{\rm line} \leqslant 15$. Note that when $N_{\rm line} > 15$, the molecular lines already contain hot-gas tracers (e.g., CH_3CN). Additionally, those with emission of lines of $N_{\rm line} \leqslant 6$ associated with CO outflows but no H30α emission are also considered candidate WCs. As a result, 971 cores (62.2%) were identified as candidate WCs (see Figure 3). Figure 4(b) shows representative molecular line spectra for a candidate WC.

3.2.2. Candidate Hot Molecular and UCHII Cores

In addition to the candidate starless cores and WCs described above, the remaining cores are assumed to be in a more advanced evolutionary stage, due to their association with detection of rich molecular line transitions ($N_{\rm line} > 15$) and/or the H30α line representative of ionized gas emission. A broad-spectrum profile of the H30α line (e.g., line width > 15 km s^{-1}, e.g., H.-L. Liu et al. 2021) and a compact emission pattern in the line-intensity map are both required to diagnose the signature of UCHII regions, as illustrated in Figure 5. Consequently, the remaining 464 cores (~30%) were classified as evolved cores (see Figure 3). As previously mentioned,

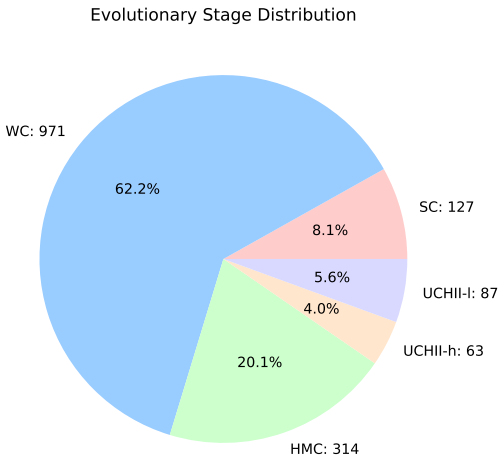

Figure 3. Pie chart for statistics of core classifications.

these evolved cores were further subdivided into three subcategories based on their associated $N_{\rm line}$ and detection of H30α (see Table 3): 314 candidate HMCs without associated H30α emission, 63 UCHII-*h* candidates with associated H30α emission and $N_{\rm line} > 15$, and 87 UCHII-*l* candidates with associated H30α emission and $N_{\rm line} \leqslant 15$ (see Figure 3). In the ATOMS survey, H.-L. Liu et al. (2021) used H40α emission to identify UCHII cores, detecting 89 sources. They also have associated H30α emission, except for two sources within I16158-5055 and I16506-4512 protocluster clumps (see Table 1 of H.-L. Liu et al. 2021) that were not covered by the QUARKS observations. The typical molecular transitions of the evolved cores are illustrated in Figures 4(c)–(e).

3.3. Physical Parameters of Dense Cores

The dust temperature ($T_{\rm dust}$) of a core is a fundamental parameter that subsequently determines other key properties of the core such as the mass and the density. However, accurately determining $T_{\rm dust}$ for individual cores within a clump remains challenging, particularly for candidate starless cores and WCs lacking detection of temperature-sensitive line transitions (e.g., CH_3CN K-ladder transitions). Besides, assigning a uniform $T_{\rm dust}$ to all cores within a clump is unrealistic due to their probable diverse evolutionary stages (see Section 3.2). Instead, we assigned $T_{\rm dust}$ for cores based on their evolutionary stage, as shown in column (3) of Table 3.

For starless cores without internal protostellar heating, dust temperatures as low as 10–15 K have been observed in IRDC environments (P. Sanhueza et al. 2013; A. T. Barnes et al. 2023; K. Morii et al. 2023; X. Mai et al. 2024). However, given the IR-bright nature of the QUARKS sample (H.-L. Liu et al. 2021; F. Xu et al. 2024b), these temperatures could be higher (e.g., ~20 K; T. Nony et al. 2018, 2023) due to external heating by nearby young stars (P. Dell'Ova et al. 2024). Therefore, we adopted here a lower limit of temperature of 20 K for all candidate starless cores, consistent not only with the assumption made in the study by the ALMA-IMF survey team (M. Valeille-Manet et al. 2025) but also with the averaged temperature measured in starless cores within clustered star-forming regions (Table 5 of Á. Sánchez-Monge et al. 2013). For the upper limit of temperature, we assigned the average $T_{\rm dust}$ of the natal clump, derived from the spectral energy distribution (S. Faúndez et al. 2004; see Table A1 in T. Liu et al. 2020).

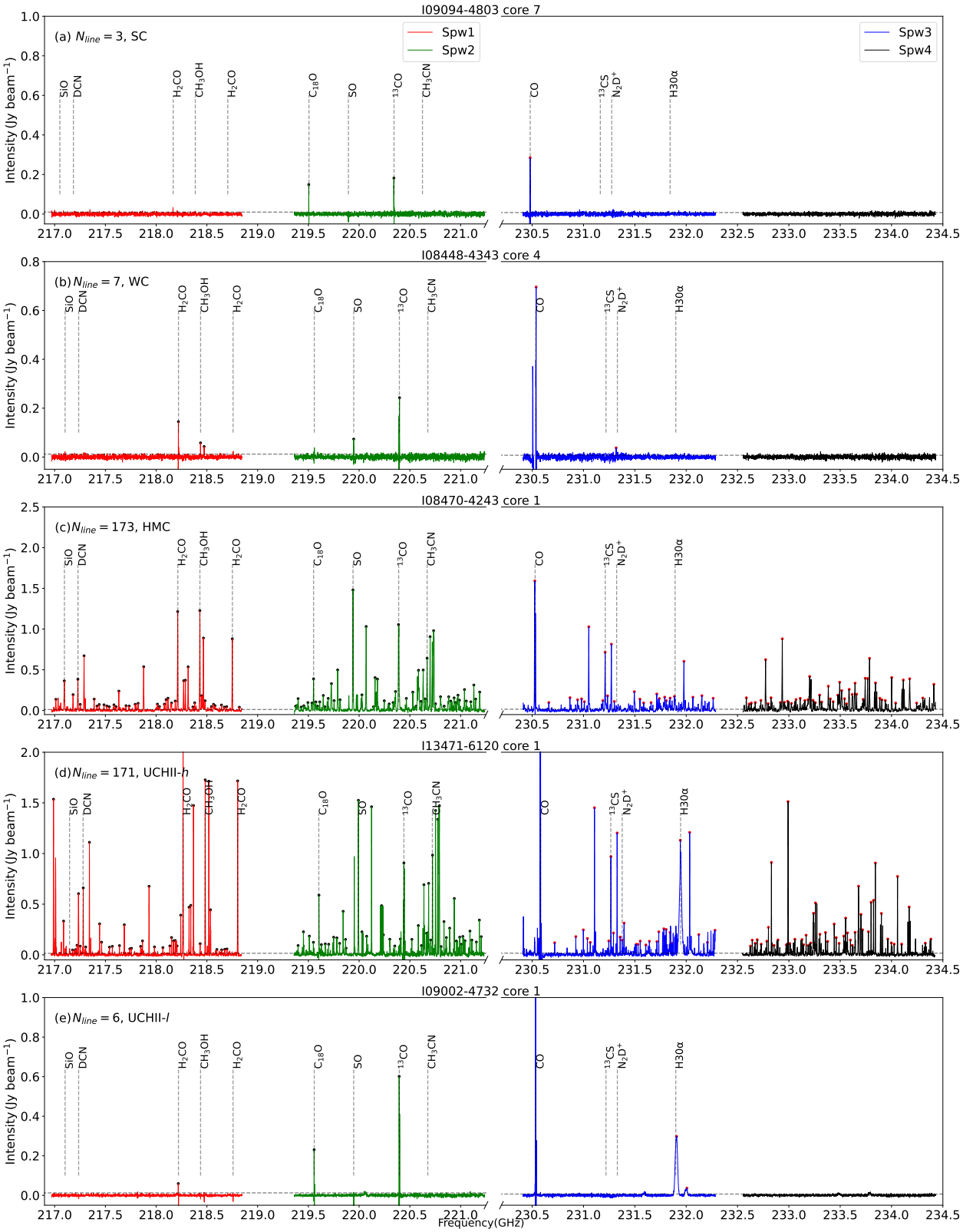

Figure 4. Demonstration of core-averaged spectra covered in the four spectral windows of the QUARKS survey for dense cores representative of different stages of evolution, including candidates of (a) starless cores, (b) warm cores, (c) hot cores, (d) UCHII-*h* cores, and (e) UCHII-*l* cores. The upper-left corner of each panel displays the count of molecular spectral lines tentatively detected in each core. The horizontal dashed line represents the noise level of the spectra. Several common molecular line transitions are labeled.

For candidate WCs, a dust temperature of 30 K was adopted (A. Traficante et al. 2023), consistent with the average $T_{\rm dust}$ ($\sim$28.6 K) of their natal clumps. Finally, for candidate evolved cores, we assumed a dust temperature of 100 K (E. Herbst & E. F. van Dishoeck 2009; S.-L. Qin et al. 2022; K. Taniguchi et al. 2023).

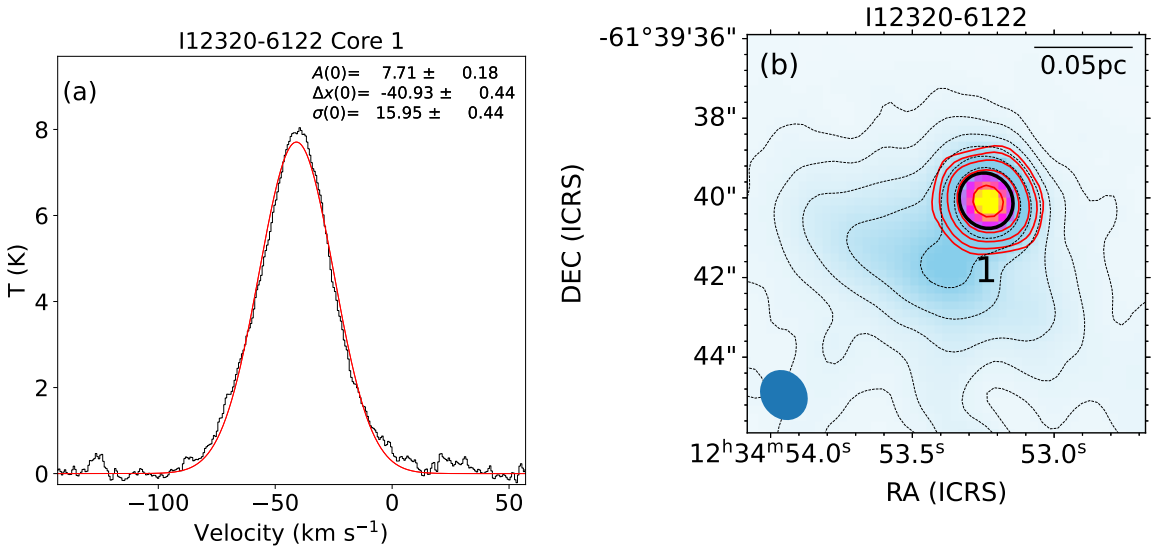

Figure 5. Emission of the H30α line toward I12320-6122 Core 1. (a) The black histogram represents the observed core-averaged spectrum while the red line is the Gaussian fitting. (b) QUARKS TM2+ACA continuum image of I12320-6122 Core 1. The contour levels are the same as in Figure 2, but with rms = 1 mJy beam^{-1}. The red contours show velocity-integrated emission of H30α over [–90, 10] km s^{-1}, with rms = 0.5 Jy beam^{-1} km s^{-1}. The black circle delineates I12320-6122 Core 1. The beam size of the TM2+ACA observations is shown on the lower left, and the 0.05 pc scale bar is on the upper-right corner.

Assuming dust continuum emission at 1.3 mm to be optically thin, the masses of the cores can be estimated as follows:

$$M_{\rm core} = \frac{S_\nu^{\rm int} D^2 R_{\rm gd}}{\kappa_\nu B_\nu(T_{\rm dust})}, \quad (1)$$

where the integrated flux ($S_\nu^{\rm int}$) is measured from 1.3 mm dust emission and D is the distance for each source, adopted from X. Liu et al. (2024). $R_{\rm gd}$ is the gas-to-dust ratio, assumed to be 100 (e.g., P. Sanhueza et al. 2019; F. Motte et al. 2022; A. Traficante et al. 2023; A. Coletta et al. 2025).[43] The dust opacity (κ_ν) is taken as 0.9 cm^2 g^{-1} (V. Ossenkopf & T. Henning 1994) and $B_\nu(T_{\rm dust})$ is the Planck function for a given $T_{\rm dust}$.

Assuming a spherical geometry, the number density of the cores was calculated as $n_{\rm H_2} = \frac{3M_{\rm core}}{4\pi R_c^3 \mu m_{\rm H}}$, where $\mu = 2.8$ is the mean molecular weight and $m_{\rm H}$ is the hydrogen atom mass (J. Kauffmann et al. 2008). The surface density is given by $\Sigma = \frac{M_{\rm core}}{\pi R_c^2}$. The deconvolved effective radius (R_c) for each core was determined using $R_c = \sqrt{(maj \times min) - (bmaj \times bmin)}/2 \times D$ (Y. Pouteau et al. 2022), where *maj* and *min* are the sizes of the major and minor axes measured by the *getsf* algorithm (see columns (6)–(7) in Table 2), and *bmaj* and *bmin* correspond to the synthesized beam dimensions of the QUARKS TM2 +ACA observations. To mitigate deconvolution artifacts, a minimum radius of half the beam size (~0.″5) was enforced, following Y. Pouteau et al. (2022).

Considering the uncertainties in distance (~10%) and dust temperature (<30%) along with that from κ_ν and $R_{\rm gd}$ (~50%; P. Sanhueza et al. 2017; X. Shen et al. 2024), we estimated the uncertainty of mass, number density, and surface density of ~50%, using the Monte Carlo approach as adopted in X. Shen et al. (2024) .

As shown in Table 4, candidate starless cores have masses (at 20 K) ranging from [0.2–21.0] $M_\odot$, with a median of 1.5 $M_\odot$, which are listed in column (8) of Table 4. Their estimated masses, calculated using the average dust temperature of their natal clumps, are listed in column (9) of Table 4. The median radius, number density, and surface density of candidate starless cores are 2800 au, 2.0 × 10^6 cm^{-3}, and 0.5 g cm^{-2}, respectively (based on a temperature of 20 K).

The physical parameters for candidate warm and evolved cores are summarized in Table 5. For candidate WCs, the median radius, number density, and surface density are 2.1 $M_\odot$, 2800 au, 2.6 × 10^6 cm^{-3}, and 0.7 g cm^{-2}, respectively. For evolved cores, the median radius, number density and surface density are 3.7 $M_\odot$, 2700 au, 5.5 × 10^6 cm^{-3}, and 1.4 g cm^{-2}. Figure 10 illustrates the distribution of physical parameters across different categories of cores studied here. Although there is a clear increase in the total flux of cores as they evolve (see Figure 10(a)), no significant differences are observed in other parameters (i.e., mass, radius, number density, and surface density, see Figures 10(b)–(e)) among cores in different evolutionary stages.

3.4. Core Separation

Dense cores form through the fragmentation of their natal molecular clump. The Jeans length and mass are commonly employed to characterize this fragmentation process. However, as noted in H. Beuther et al. (2018), mass estimates are subject to significant uncertainties—not only from missing flux but also from assumptions about dust properties and temperatures (introducing uncertainties with factors of about 2, see Section 3.3). Consequently, core separation could serve as a more suitable proxy for analyzing fragmentation properties in clumps.

The minimum-spanning tree (MST; J. D. Barrow et al. 1985; S. Dib & T. Henning 2019) method was used to determine the shortest separation between the cores within each clump (see Figure 6 for two illustrative examples). This approach has been

[43] Other values for $R_{\rm gd}$ can be found in the literature, ranging from 110–150 (e.g., H. Beuther et al. 2018; B. E. Svoboda et al. 2019; A. T. Barnes et al. 2021, 2023). This implies an $R_{\rm gd}$ uncertainty of ~50%.

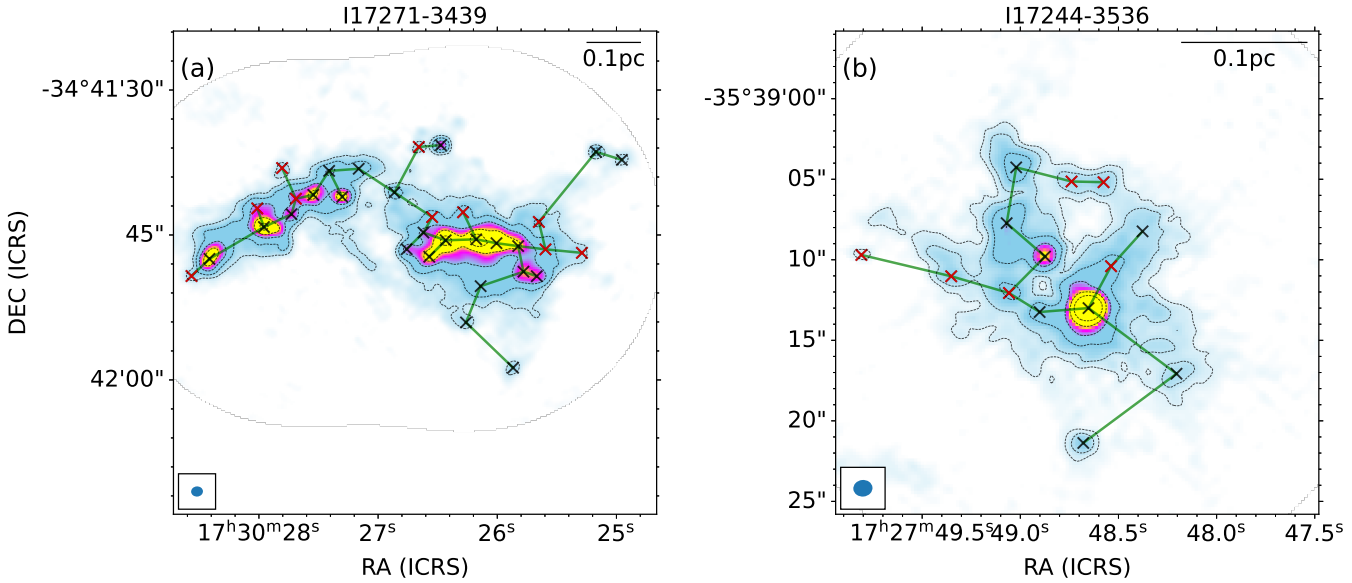

Figure 6. Example of the MST results (green segments). QUARKS TM2+ACA 1.3mm continuum emission is shown in a color scale with dense cores (i.e., cross symbols) overlaid. The contour levels are the same as in Figures 2(b) and (d). The beam size of the QUARKS data is shown on the lower left, and the 0.1 pc scale bar is on the upper right.

widely applied in studies of star-forming filaments, fibers, and clumps for core separation analysis (K. Wang et al. 2016; P. Sanhueza et al. 2019; S. Zhang et al. 2021; H.-L. Liu et al. 2022a; K. Morii et al. 2023; K. Ishihara et al. 2024; K. Morii et al. 2024; F. Xu et al. 2024a; D. Yang et al. 2024).

Figure 7(a) presents the angular separation distribution for all cores in this study, spanning [0.9, 17.9]″ (corresponding to [0.005, 0.72] pc). The distribution peaks at 2.″5 (black dashed line in Figure 7(a)), about twice the QUARKS TM2+ACA resolution (∼1″), regardless of the source distance. This result suggests that all individual cores within each clump can be resolved well by current angular resolution.

In Figure 7(b), the linear separation distribution exhibits a strong dependence on the source distance, with the median separation shifting toward higher values for farther distances (see the specific values in the legend of the figure, and also Figure 11). This reflects an observational effect rather than a physical phenomenon, arising from the QUARKS survey's varying absolute mass sensitivity and linear resolution. For instance, the minimum detectable core mass increases with distance (Figure 12(a)), while the number of core detections (surface density of the core count) decreases systematically with distance (Figure 12(b)). These effects naturally lead to greater linear separations for more distant sources.

It should be noted that the measured core separations could represent lower limits due to projection effects, with actual values being potentially 1–2 times greater.

3.5. Analysis of Thermal Jeans Length

To investigate the clump-to-core fragmentation using the QUARKS TM2+ACA continuum data, we conducted the comparison between the observed linear separation of the cores and the predicted thermal Jeans length within their natal clumps. Using physical parameters from Table A1 in T. Liu et al. (2020), we find that the clump number densities range from $\sim 10^3$–10^5 cm^{-3} and the dust temperatures vary between 19.5 and 45.5 K. These conditions yield Jeans lengths

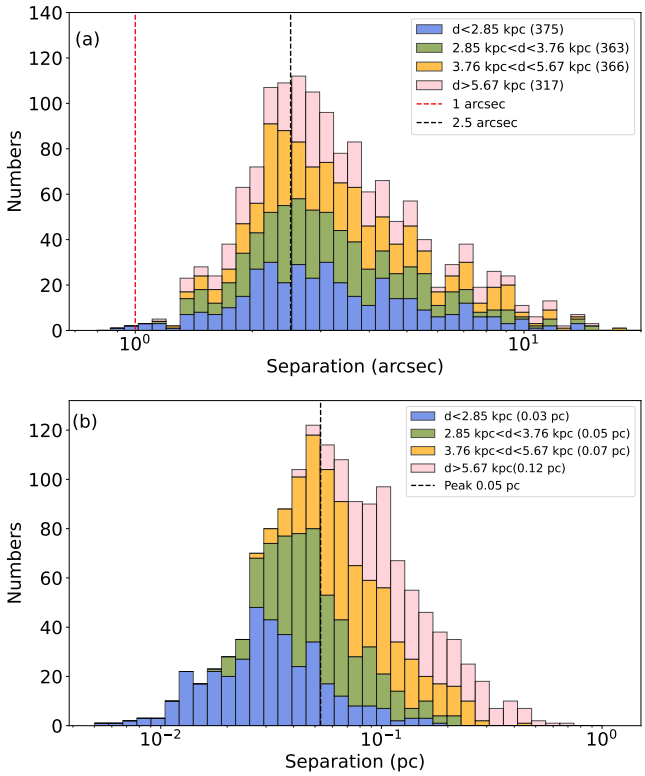

Figure 7. Distributions of core separation within all QUARKS protocluster clumps. To visualize the distance effect on the distribution, the clumps were devided into four quartile groups based on their measured distances: ⩽2.85, (2.85–3.76), (3.76–5.67), and ⩾5.67 kpc, with each quartile coded by a distinct color. The count of the corresponding groups is 36, 35, 35, and 35 protocluster clumps, respectively. (a) Distribution of the angular separation. The number of core separation measurements for each group of protocluster clumps is 375, 363, 366, and 317, respectively, as shown in upper-right legend. The black and red dashed lines indicate the peak of the distribution (∼2.″5), and the typical beam size (∼1″) of our observations, respectively. (b) Distribution of the linear core separation. The median value of the distribution for each group of protocluster clumps is 0.03, 0.05, 0.07, and 0.12 pc, respectively, as shown in upper-right legend. The black dashed line indicates the peak of this distribution.

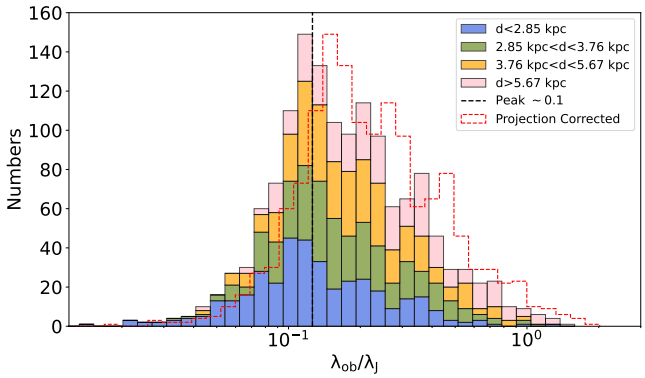

Figure 8. Distribution of the ratio between the observed core separation to the predicted thermal Jeans length. The black dashed line shows the peak of the distribution. The red contour represents the distribution with the spatial projection correction applied (see text).

($\lambda_J = c_s(\pi/G\rho)^{1/2}$) of ∼[0.07, 1.1] pc for all clumps of the QUARKS survey.

The ratio of the observed core separation to the thermal Jeans length (λ_{obs}/λ_J) is shown in Figure 8, revealing a distribution apparently independent of the source distance. Both λ_{obs} and λ_J exhibit positive correlations with source distance, as demonstrated by Spearman's rank correlation tests:[44] $\rho_s \sim 0.9$ ($p \ll 0.01$) for the λ_{obs} in Figure 11, and $\rho_s \sim 0.6$ ($p \ll 0.01$) for the λ_J in Figure 13(a). However, the λ_{obs}/λ_J ratio can effectively mitigate (or reduce) the effects related to the source distance, as illustrated in Figure 13(b) ($\rho_s \sim 0.4$ and $p \ll 0.01$). Almost all ratios (∼99%, 1407/1421) are below 1, peaking at ∼0.1 (black dashed line in Figure 8). After applying the correction for projection effects (consider the factor of $4/\pi$, e.g., K. Ishihara et al. 2024), the red histogram in Figure 8 shows that ∼98% (1391/1421) of the ratios remain below unity, with a peak at ∼0.2. This result indicates that the massive protocluster clumps studied here fragment with core separations significantly smaller than the predicted thermal Jeans lengths. This agrees with recent studies showing observed core separations comparable to or less than the thermal Jeans length both in IRDCs (P. Sanhueza et al. 2019; K. Morii et al. 2024), and in more evolved IR-bright star-forming clumps (A. Palau et al. 2015, 2018; H. Beuther et al. 2018; S. Zhang et al. 2021; K. Ishihara et al. 2024).

Interestingly, a secondary peak in Figure 8 appears at $\lambda_{obs}/\lambda_J \sim 0.3$. A similar bimodal distribution of core separations has also been observed (P. S. Teixeira et al. 2016; A. Palau et al. 2018; B. E. Svoboda et al. 2019; S. Zhang et al. 2021), which could be attributed to hierarchical fragmentation occurring at two distinct scales within a clump. Note that the secondary peak is much weaker than the primary one, and thus should be treated with caution.

4. Discussion

4.1. Fragmentation of Protocluster Clumps

Recent high-angular-resolution ALMA observations suggest that fragmentation of both IR-dark and IR-bright clumps could follow the thermal Jeans fragmentation mechanism. For instance, in the ALMA-ASHES survey targeting tens of IRDC clumps, core separations align with the predicted thermal Jeans length, while core masses fall below the thermal Jeans mass (P. Sanhueza et al. 2019; K. Morii et al. 2024). Similar results were observed in evolved protocluster clumps (A. Palau et al. 2015; H. Beuther et al. 2018; S. R. Das et al. 2024) and those associated H II region environments (S. Zhang et al. 2021). Our QUARKS sample, which includes IR-bright massive protocluster clumps more evolved than the ASHES sample (F. Xu et al. 2024b), with most hosting embedded UCHII sources (H.-L. Liu et al. 2021; S. Zhang et al. 2023b; C. Zhang et al. 2024), shows core separations significantly smaller than the corresponding thermal Jeans length ($\lambda_{obs}/\lambda_J \sim 0.2$, accounting for projection effects). This suggests that the IR-bright protocluster clumps in our study fragment primarily through thermal Jeans fragmentation.

Moreover, the peak of the core separation distribution at ∼0.05 pc (Figure 7(b)) agrees with that observed in other IR-bright massive clumps (∼0.04 pc; see Figure 6 of F. Xu et al. 2024a) but is significantly less than those measured in IR-dark massive clumps (∼0.1 pc; P. Sanhueza et al. 2019; K. Morii et al. 2023). This difference in typical core separations between IR-dark and IR-bright clumps could naturally lead to the observed low ratio of $\lambda_{obs}/\lambda_J \sim 0.2$. This result could be linked to the evolutionary stage of the natal clumps, as suggested by recent studies (H. Beuther et al. 2018; A. Traficante et al. 2023). Specifically, dense cores could initially form via thermal Jeans fragmentation during the IR-dark stage with slightly larger separations, and then evolve toward fewer separations due to the persistent global gravitational collapse and contraction over time (P. S. Teixeira et al. 2016; F. Xu et al. 2024a; S. R. Das et al. 2024). However, when using the luminosity-to-mass ratio (L/M) as an evolutionary indicator (e.g., H.-L. Liu et al. 2021) for the QUARKS protocluster clumps, we do not find a clear correlation between the L/M and core separation, which is not shown here. This lack of correlation could stem from a limited dynamical range of evolutionary phases in the QUARKS sample, which includes IR-bright stages only. Additionally, as protocluster clumps evolve, they could generate new fragments, leading to a reduction in core separations over time, as reported in recent studies using ALMAGAL survey data at ∼1000 au resolution (A. Coletta et al. 2025).

An alternative explanation for the observed $\lambda_{obs}/\lambda_J \sim 0.2$ significantly below unity could be due to the existence of a hierarchical fragmentation mode within the clumps. Through this mode, massive protocluster clumps initially fragment into subclumps, which subsequently break down hierarchically into smaller-scale dense cores (K. Morii et al. 2024). As a first approximation, considering that the number densities of subclumps in the QUARKS survey to be those derived from the ACA compact sources (i.e., $\sim 10^5$–10^6 cm^{-3}, F. Xu et al. 2024b), the Jeans lengths within subclumps would decrease by a factor of ∼3–10 with respect to those within their larger-scale natal clumps as analyzed in Section 3.5. This would shift the peak of the λ_{obs}/λ_J distribution in Figure 8 to ∼0.3–1, which still agrees with the thermal Jeans fragmentation mechanism well. Future detailed investigations into hierarchical fragmentation involving (sub)clump scales based on the QUARKS survey are required (W. Y. Jiao et al. 2025, in preparation). Overall, regardless of the potential evolution of

[44] The Spearman's rank correlation test is suitable for small sample sizes and does not require the variables to follow a Gaussian (normal) distribution. A ρ_s closer to +1 or −1 indicates a stronger positive or negative monotonic relationship, respectively, and the value of 0 suggests no correlation. If p-value < 0.01, the result is considered statistically significant.

the core separation with the clump evolutionary stage and likely existence of a hierarchical fragmentation mode, the observed low ratio of $\lambda_{\rm obs}/\lambda_{\rm J} \ll 1$ indicates that the massive protocluster clumps investigated here are undergoing thermal Jeans fragmentation.

Unlike our findings, some studies found that in IR-dark clumps there are dense core masses exceeding the thermal Jeans mass by at least an order of magnitude, consistent with expectations for turbulent Jeans fragmentation of their natal clumps (Q. Zhang et al. 2009; Q. Zhang & K. Wang 2011; P. Sanhueza et al. 2013; K. Wang et al. 2014). As noted in other studies, this discrepancy may arise either from observational limitations—such as insufficient mass sensitivity ($>2M_{\odot}$) and spatial resolution (>5000 au) (A. Palau et al. 2015)—or from the fact that low-mass cores (or fragments) do not form yet at such early evolutionary stages (K. Wang et al. 2014; Q. Zhang et al. 2015). Alternative explanations for this discrepancy include steep initial density profiles (e.g., $\rho \propto r^{-1.5}$ or $\rho \propto r^{-2}$), which favor the formation of central massive cores (P. Girichidis et al. 2011; A. Palau et al. 2014). Additionally, stronger magnetic fields have been proposed to suppress fragmentation and promote massive core formation (S. Dib et al. 2007; B. Commerçon et al. 2011; T. Pillai et al. 2011; F. Fontani et al. 2016; P. Hennebelle et al. 2022). However, recent studies have argued that strong magnetic fields do not reverse the thermal Jeans fragmentation process but instead act as a modulating factor (e.g., A. Palau et al. 2021; K. S. Klos et al. 2025) that facilitates the formation of a few high-mass stars (e.g., P. Saha et al. 2024; P. Sanhueza et al. 2025). In the future, systematic investigations using the QUARKS sample will be essential to clarify the influence of these factors on clump fragmentation.

4.2. Comparison with ATOMS' "Unknown" Source Catalog

In the ATOMS survey, H.-L. Liu et al. (2021) identified 280 compact fragments lacking signatures of HMCs or UCHII regions, designating them as ATOMS' "unknown" sources. These sources exhibit median properties of 2.4×10^{-2} pc radius in an interquartile range (IQR) of $[1.4, 4.6] \times 10^{-2}$ pc, $63\,M_{\odot}$ mass in an IQR of $[20, 320]\,M_{\odot}$, $9 \times 10^{6}\,{\rm cm^{-3}}$ number density in an IQR of $[4, 17] \times 10^{6}\,{\rm cm^{-3}}$ and $7.2\,{\rm g\,cm^{-2}}$ mass surface density in an IQR of $[4.3, 14.2]\,{\rm g\,cm^{-2}}$. Due to these characteristics of high mass and density, H.-L. Liu et al. (2021) suggested that the "unknown" sources might represent precursors to high-mass star formation. We crossmatched the ATOMS "unknown" sources sample with the 1562 QUARKS TM2+ACA cores from this study (Figure 9). Of the 280 "unknown" sources, 69 lie outside the QUARKS survey field, while the remaining 211 correspond to 464 QUARKS cores. This suggests that each "unknown" source could fragment into at least two QUARKS cores at $\sim$1″ resolution. The majority of the "unknown" sources sample (75%, 157/211) harbor candidate starless cores and/or WCs, while 25% (54/211) contain evolved cores. This indicates that the catalog of ATOMS' "*unknown*" sources is a suitable sample to investigate initial conditions of high-mass star formation. In particular, 16 of these ATOMS "unknown" sources are uniquely linked to candidate starless cores within the QUARKS TM2+ACA catalog (see Figure 9), suggesting their potential as prime candidates in the initial phases of high-mass star formation core evolution and thus highlighting the strong need for detailed follow-up studies.

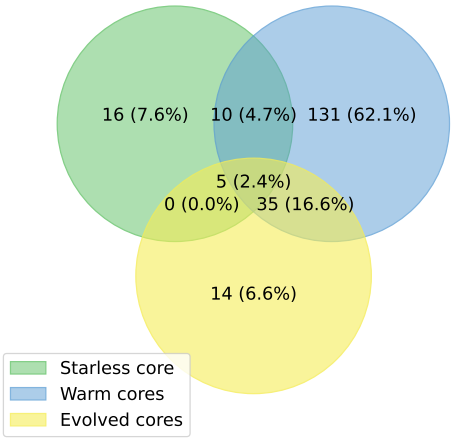

Figure 9. Venn diagram of crossmatched ATOMS "*unknown*" sources with QUARKS TM2+ACA cores at different evolutionary stages. The number in each circle represents the crossmatched result.

4.3. Searching for Candidate High-mass Starless Cores and Implications for High-mass Star Formation

Competitive accretion-type models predict that a massive clump fragments into numerous low-mass cores that subsequently promote high-mass star formation through competitive gas accretion (I. A. Bonnell et al. 2001) within the clump and even beyond (E. Vázquez-Semadeni et al. 2019; P. Padoan et al. 2020). In contrast, the existence of individual high-mass starless cores is crucial for validating turbulent core accretion-type models (C. F. McKee & J. C. Tan 2003). To date, only a handful of candidate high-mass starless cores have been identified (K. Wang et al. 2014; T. Liu et al. 2017; A. T. Barnes et al. 2023; T. Nony et al. 2023; X. Mai et al. 2024; M. Valeille-Manet et al. 2025).

In this study, we classified 127 candidate starless cores. Assuming a star formation efficiency of 50% as adopted in T. Nony et al. (2018) and M. Valeille-Manet et al. (2025), only two candidates (with $M_{\rm core} \geqslant 16\,M_{\odot}$ at $T_{\rm d} = 20$ K) could potentially form high-mass stars independently. We highlight these two cores in boldface in Table 4, which have radii of 5000–7000 au and masses of 17–21 $M_{\odot}$. The virial parameter ($\alpha_{\rm vir} = 5\sigma_{\rm eff}^2 R_c/{\rm G}\,M_{\rm c}$, F. Bertoldi & C. F. McKee 1992) is widely used to evaluate the dynamical state of a core (e.g., H.-L. Liu et al. 2021; A. T. Barnes et al. 2021; F. Xu et al. 2024a; M. Valeille-Manet et al. 2025). Considering typical total velocity dispersions of high-mass prestellar cores in the literature ($\sim$0.4–0.8 km s^{-1}, e.g., A. T. Barnes et al. 2023; X. Mai et al. 2024), we find $\alpha_{\rm vir} < 2$ for the two candidates studied here. This indicates that they are gravitationally bound and could be therefore candidate prestellar cores, precursors of high-mass star formation. Line spectra of the two candidate cores and detection maps of CO outflows within their natal clumps are shown in Figures 14 and 15, respectively.

It is worth noting that the number of high-mass starless candidates identified here likely represents a lower limit. First, if a lower dust temperature was considered (10–15 K, e.g., F. Motte et al. 2018; A. T. Barnes et al. 2023; K. Morii et al. 2023; X. Mai et al. 2024), this would shift the masses of six cores (i.e., 8–16 $M_{\odot}$ at 20 K) to values greater than 16 $M_{\odot}$, potentially adding additional high-mass starless candidates. Second, QUARKS' high-angular-resolution observations at 1.3 mm primarily trace dense kernels of cores, likely significantly filtering out their envelope mass. In contrast,

the ATOMS survey observations at 3 mm at a lower angular resolution retain relatively more extended envelope emission (X. Mai et al. 2024). As illustrated in Figure 16, the ATOMS "unknown" sources exhibit significantly larger median size and mass than the QUARKS candidate starless cores studied here, with the difference on the median size and mass by factors of ∼3 and ∼50, respectively. Note that only 26 ATOMS "unknown" sources that are crossmatched with the QUARKS candidate starless cores (see Figure 9) are depicted in Figure 16. Future studies combining QUARKS and ATOMS data are therefore needed to better evaluate the mass threshold for potential high-mass starless candidates. Furthermore, there could be potential high-mass starless cores in our WC catalog, arising from those ∼5% (∼50/971) cores with $M_{\rm core} \geqslant 8\,M_{\odot}$ at $T_{\rm d} = 30$ K (see Appendix A) that are not associated with any star-forming signatures (e.g., outflows).

Regardless of the precise candidate count, we find that 90% of candidate starless cores ($M_{\rm core} \leqslant 8\,M_{\odot}$) lack sufficient mass for monolithic high-mass star formation. However, surrounding filaments and streamers may channel gas mass onto these cores (A. Saha et al. 2022; J.-W. Zhou et al. 2022; D. Yang et al. 2023; F.-W. Xu et al. 2023), enabling future high-mass star formation (F. Motte et al. 2018) as depicted in the competitive accretion model. Our results therefore require competitive accretion-like models where clumps first fragment into low-mass cores and high-mass stars primarily grow through multiscale dynamical mass accretion from beyond their immediate gas reservoir, with rare cases forming via monolithic collapse with associated mass accretion onto protostars from the envelope of their natal massive starless cores.

5. Summary

The QUARKS survey observed 139 IR-bright massive star-forming protocluster clumps across 156 pointings using ALMA band 6 (∼ 1.3 mm). These observations employed three configurations of the ALMA 12 m array: C-5 (TM1, ∼0.″3), C-2 (TM2, ∼1″), and ACA 7 m array (∼5″). This study details the imaging procedures to generate the continuum and line data sets from the combined TM2+ACA observations. Employing self-calibration in both continuum and line imaging, the final reduced TM2+ACA combined data achieved an average noise level of ∼0.6 mJy beam^{-1} with a synthesized beam of ∼1.″3 × 1.″1 for continuum, and an average noise level of ∼10 mJy beam^{-1} per channel at a velocity resolution of ∼1.3 km s^{-1} and a synthesized beam of ∼1.″4 × 1.″1 for spectral lines.

Furthermore, 1562 compact cores were extracted from the TM2+ACA combined continuum data using the *getsf* algorithm. Using these cores, we conducted a systematic investigation into clump-to-core fragmentation and a preliminary search for candidate high-mass starless cores. The major findings are summarized below.

Based on associated star-forming signatures, namely the richness of molecular transitions ($N_{\rm line}$), outflows, and/or ionized gas tracers, we categorized the identified cores into three groups: 127 candidate starless cores, 971 candidate WCs, and 464 candidate evolved cores. The evolved candidates consist of three subcategories: 314 candidate HMCs, 63 candidate UCHII-*h* cores (UCHII-*h*) with high $N_{\rm line}$, and 87 candidate UCHII-*l* cores (UCHII-*l*) with low $N_{\rm line}$. The median size, mass, and surface density were estimated as follows: 2900 au, 1.6 $M_{\odot}$, and 0.6 g cm^{-2} for candidate starless cores; 2600 au, 2.0 $M_{\odot}$, and 0.7 g cm^{-2} for candidate WCs; 2700 au, 3.7 $M_{\odot}$, and 1.4 g cm^{-2} for evolved cores.

Employing the MST method, we quantified the core separations within each protocluster clump. The angular separations of all cores range from 0.″9 to 17.″9, peaking at 2.″5, approximately twice the TM2+ACA resolution (∼1″), indicating that the studied cores are spatially resolved well. In contrast, the distribution of the linear core separation, spanning [0.005, 0.72] pc and peaking at ∼0.05 pc, shows a strong positive correlation with the source distance, with the core separation increasing toward a far distance.

Moreover, the observed linear core separations ($\lambda_{\rm obs}$) within each clump are much less than the related theoretical thermal Jeans length ($\lambda_{\rm J}$), yielding a ratio of $\lambda_{\rm obs}/\lambda_{\rm J} \sim 0.2$ when accounting for projection effects. This finding indicates that the massive protocluster clumps in this study are undergoing thermal Jeans fragmentation. We further suggest that the observed low ratio of $\lambda_{\rm obs}/\lambda_{\rm J} \ll 1$ could stem from either the potential evolution of core separation with the clump's evolutionary stage or the likely presence of hierarchical fragmentation within clumps.

The IR-bright environment of massive protocluster clumps, characterized by typically higher gas temperatures compared to IR-dark regions, may foster the formation of high-mass starless cores. Within 127 candidate starless cores revealed in QUARKS TM2+ACA continuum emission, we identified two cores exceeding 16 $M_{\odot}$ as high-mass candidates, possessing radii of 3000–8000 au and masses of 17–21 $M_{\odot}$. The number of such candidates identified here represents a lower limit due to the inherent mass estimate uncertainty of the cores, which warrants further investigation for starless cores by integrating the ATOMS and QUARKS data sets. Irrespective of the exact candidate count, we find that 90% of candidate starless cores ($M_{\rm core} \leqslant 8\,M_{\odot}$) do not possess sufficient mass for monolithic high-mass star formation. The scarcity of such high-mass starless candidates therefore suggests that competitive accretion-like models are more applicable than turbulent core accretion-like models in high-mass star formation within the IR-bright protocluster clumps studied here.

Acknowledgments

This work has been supported by the National Key R&D Program of China (No. 2022YFA1603101), the National Natural Science Foundation of China (NSFC) through grant Nos. 12073061, 12122307, and 12033005. H.-L.L. is supported by the Yunnan Fundamental Research Project (grant Nos. 202301AT070118, 202401AS070121), and by the Xingdian Talent Support Plan–Youth Project. D.Y. is supported by the Scientific Research Fund Project of Yunnan Education Department (Project ID: 2025Y0106, KC-24248416). T.L. acknowledges the support from the PIFI program of Chinese Academy of Sciences through grant No. 2025PG0009, and the Tianchi Talent Program of Xinjiang Uygur Autonomous Region. S.Z. gratefully acknowledges support by the CAS-ANID project CAS220003. X.L. has also been supported by CPSF No. 2022M723278. P.S. was partially supported by a Grant-in-Aid for Scientific Research (KAKENHI number JP22H01271 and JP23H01221) of the Japan Society for the Promotion of Science (JSPS). A.M.S. gratefully acknowledges support by the Fondecyt Regular (project code 1220610), and ANID BASAL project FB210003. G.G. gratefully

acknowledges support by the ANID BASAL project FB210003. T.Z. acknowledges the National Natural Science Foundation of China (grant No. 12373026), the Leading Innovation and Entrepreneurship Team of Zhejiang Province of China (grant No. 2023R01008), and the China Postdoctoral Science Foundation (grant No. 2023TQ0330). S.R.D. acknowledges support from the Fondecyt Postdoctoral fellowship (project code 3220162) and ANID BASAL project FB210003. K.T. is supported by JSPS KAKENHI grant Nos. 21H01142, 24K17096, and 24H00252. L.B. gratefully acknowledges support by the ANID BASAL project FB210003. A.P. acknowledges financial support from the UNAM-PAPIIT IG100223 grant, the Sistema Nacional de Investigadores of SECIHTI, and from the SECIHTI project number 86372 of the "Ciencia de Frontera 2019" program, entitled "Citlalcóatl: A multiscale study at the new frontier of the formation and early evolution of stars and planetary systems", Mexico. A.H. thanks the support from the S. N. Bose National Centre for Basic Sciences under the Department of Science and Technology, Govt. of India and the CSIR-HRDG, Govt. of India for the funding of the fellowship. This work was performed in part at the Jet Propulsion Laboratory, California Institute of Technology, under contract with the National Aeronautics and Space Administration. This paper makes use of the following ALMA data: ADS/JAO. ALMA#2021.1.00095.S.

Appendix A
Physical Parameters of the QUARKS TM2+ACA Dense Cores

Derived parameters for candidate starless cores are listed in Table 4, and those for candidate warm and evolved cores are presented in Table 5. Figure 10 presents the distribution of physical parameters for dense cores across different evolutionary stages. While the total flux of cores generally increases with evolutionary stage, mass, radius, and number density do not show clear trends. Note that 27 cores exceeding 100 $M_\odot$ (Figure 10(b)) are evolved cores (11 in HMCs and 15 in UCHII cores), which require careful consideration due to their association with ionized gas emission. From the cross-match between these cores and MeerKAT 1.3 GHz radio continuum arising from free–free emission, we find that except for the UCHII cores, almost all HMCs in question lie in extended ionized gas emission. The 1.3 mm flux of these 27 cores could be significantly affected by free–free emission, potentially leading to mass overestimation.

Table 4
Derived Parameters for Candidate Starless Cores

Source	Core	RA (IRCS) (h:m:s)	Decl. (IRCS) (d:m:s)	R (au)	$N_{\rm line}$[a]	Temp.[b] (K)	Mass$_{\rm upper}$[c] ($M_\odot$)	Mass$_{\rm lower}$[c] ($M_\odot$)	$n_{\rm H_2(20\,K)}$[d] ($\times 10^6$ cm^{-3})	$\Sigma_{\rm (20\,K)}$[d] (g cm^{-2})
(1)	(2)	(3)	(4)	(5)	(6)	(7)	(8)	(9)	(10)	(11)
I08448-4343	9	$8^h46^m31\overset{s}{.}99$	$-43^d54^m40\overset{s}{.}07$	535	5	25	0.3	0.23	59.3	3.0
I08448-4343	20	$8^h46^m33\overset{s}{.}89$	$-43^d54^m27\overset{s}{.}39$	744	2	25	0.21	0.16	15.4	1.1
I09002-4732	8	$9^h01^m54\overset{s}{.}91$	$-47^d44^m01\overset{s}{.}87$	628	6	39	1.21	0.54	147.9	8.7
I09094-4803	6	$9^h11^m08\overset{s}{.}68$	$-48^d16^m04\overset{s}{.}62$	8752	3	23	7.01	5.86	0.3	0.3
I09094-4803	7	$9^h11^m08\overset{s}{.}87$	$-48^d16^m04\overset{s}{.}12$	6003	3	23	2.9	2.43	0.4	0.2
I09094-4803	9	$9^h11^m08\overset{s}{.}61$	$-48^d15^m51\overset{s}{.}44$	4234	4	23	2.26	1.89	0.9	0.4
I12572-6316_2	3	$13^h00^m28\overset{s}{.}74$	$-63^d32^m29\overset{s}{.}79$	7832	2	21	10.93	10.26	0.7	0.5
I12572-6316_2	4	$13^h00^m28\overset{s}{.}11$	$-63^d32^m38\overset{s}{.}47$	10540	4	21	12.76	11.98	0.3	0.3
I13079-6218	5	$13^h11^m08\overset{s}{.}42$	$-62^d34^m44\overset{s}{.}89$	2070	3	28	4.71	3.09	16.1	3.1
I13079-6218	6	$13^h11^m09\overset{s}{.}29$	$-62^d34^m41\overset{s}{.}35$	2009	5	28	3.33	2.18	12.4	2.3
I13111-6228	11	$13^h14^m28\overset{s}{.}01$	$-62^d44^m27\overset{s}{.}77$	1570	4	30	0.49	0.3	3.8	0.6
I13134-6242	3	$13^h16^m42\overset{s}{.}27$	$-62^d58^m26\overset{s}{.}40$	1853	4	29	1.33	0.84	6.3	1.1
I13140-6226	12	$13^h17^m16\overset{s}{.}14$	$-62^d42^m34\overset{s}{.}20$	3419	5	22	1.57	1.39	1.2	0.4
I13291-6229	10	$13^h32^m30\overset{s}{.}46$	$-62^d45^m07\overset{s}{.}80$	3787	2	28	1.32	0.86	0.7	0.3
I13291-6229	12	$13^h32^m30\overset{s}{.}53$	$-62^d45^m10\overset{s}{.}99$	3624	2	28	0.71	0.47	0.5	0.2
I13291-6229	13	$13^h32^m35\overset{s}{.}50$	$-62^d45^m33\overset{s}{.}33$	2479	2	28	0.69	0.45	1.4	0.3
I13295-6152	7	$13^h32^m53\overset{s}{.}25$	$-62^d07^m56\overset{s}{.}08$	3310	2	19	1.24	1.16	1.0	0.3
I13295-6152	10	$13^h32^m53\overset{s}{.}39$	$-62^d07^m52\overset{s}{.}41$	1443	4	19	0.19	0.17	1.7	0.2
I14050-6056	7	$14^h08^m41\overset{s}{.}68$	$-61^d10^m46\overset{s}{.}60$	2558	4	32	1.21	0.68	2.2	0.5
I14050-6056	9	$14^h08^m42\overset{s}{.}79$	$-61^d10^m42\overset{s}{.}40$	1844	3	32	0.68	0.38	3.3	0.6
I14206-6151	2	$14^h24^m23\overset{s}{.}03$	$-62^d05^m21\overset{s}{.}32$	1579	3	27	0.87	0.6	6.7	1.0
I14206-6151	5	$14^h24_m23\overset{s}{.}72$	$-62^d05^m12\overset{s}{.}31$	2781	3	27	0.96	0.66	1.4	0.4
I14206-6151	6	$14_h24^m24\overset{s}{.}11$	$-62^d05^m25\overset{s}{.}30$	3263	4	27	0.52	0.35	0.5	0.1
I14212-6131	5	$14^h25^m03\overset{s}{.}85$	$-61^d44^m44\overset{s}{.}95$	2431	5	21	2.64	2.48	5.6	1.3
I14212-6131	11	$14^h24^m59\overset{s}{.}40$	$-61^d45^m04\overset{s}{.}12$	3031	4	21	1.28	1.21	1.4	0.4
I15384-5348	6	$15^h42^m16\overset{s}{.}81$	$-53^d58^m28\overset{s}{.}69$	2969	3	33	1.28	0.69	1.5	0.4
I15384-5348	8	$15^h42^m17\overset{s}{.}14$	$-53^d58^m35\overset{s}{.}86$	2851	4	33	1.73	0.93	2.3	0.6
I15384-5348	9	$15^h42^m17\overset{s}{.}44$	$-53^d58^m35\overset{s}{.}69$	2484	3	33	1.45	0.78	2.9	0.7
I15384-5348	10	$15^h42^m17\overset{s}{.}31$	$-53^d58^m37\overset{s}{.}69$	1937	3	33	0.97	0.52	4.0	0.7
I15384-5348	15	$15^h42^m17\overset{s}{.}22$	$-53^d58^m33\overset{s}{.}80$	2037	4	33	0.96	0.52	3.4	0.7
I15411-5352	15	$15^h44^m59\overset{s}{.}11$	$-54d02^m13\overset{s}{.}48$	3646	3	30	1.51	0.91	0.9	0.3
I15437-5343	2	$15^h47^m34\overset{s}{.}01$	$-53^d52^m34\overset{s}{.}70$	2665	3	29	2.59	1.63	4.1	1.0
I15437-5343	5	$15^h47^m32\overset{s}{.}02$	$-53^d52^m34\overset{s}{.}12$	3839	4	29	2.86	1.8	1.5	0.5
I15502-5302[e]	**3**	$\mathbf{15^h54^m05\overset{s}{.}28}$	$\mathbf{-53^d11^m40\overset{s}{.}04}$	**4894**	**3**	**35**	**20.97**	**10.55**	**5.4**	**2.5**
I15522-5411	8	$15^h56^m09\overset{s}{.}31$	$-54^d19^m32\overset{s}{.}17$	1369	6	23	0.31	0.26	3.7	0.5

Table 4
(Continued)

Source	Core	RA (IRCS) (h:m:s)	Decl. (IRCS) (d:m:s)	R (au)	N_{line}[a]	Temp.[b] (K)	$Mass_{upper}$[c] ($M_\odot$)	$Mass_{lower}$[c] ($M_\odot$)	$n_{H_2(20\,K)}$[d] ($\times 10^6$ cm^{-3})	$\Sigma_{(20\,K)}$[d] (g cm^{-2})
(1)	(2)	(3)	(4)	(5)	(6)	(7)	(8)	(9)	(10)	(11)
I15570-5227	8	16h00m55.s44	−52d36m27.s11	4715	2	28	3.64	2.39	1.1	0.5
I15570-5227	11	16h00m55.s17	−52d36m21.s93	3535	3	28	1.04	0.68	0.7	0.2
I16026-5035	4	16h06m25.s77	−50d43m22.s44	2730	1	31	3.63	2.11	5.4	1.4
I16026-5035	6	16h06m22.s75	−50d43m35.s50	3571	4	31	3.02	1.75	2.0	0.7
I16026-5035	14	16h06m25.s95	−50d43m11.s90	3169	4	31	1.5	0.87	1.4	0.4
I16037-5223	9	16h07m38.s60	−52d31m06.s77	6544	4	31	6.47	3.76	0.7	0.4
I16132-5039	5	16h17m01.s26	−50d46m47.s01	2544	5	32	1.66	0.93	3.1	0.7
I16132-5039	9	16h17m00.s73	−50d46m47.s22	2154	5	32	0.81	0.45	2.5	0.5
I16132-5039	10	16h17m02.s83	−50d46m44.s45	2224	4	32	0.66	0.37	1.8	0.4
I16132-5039	12	16h17m00.s56	−50d46m46.s57	2813	6	32	1.25	0.7	1.7	0.4
I16132-5039	20	16h17m01.s82	−50d46m54.s25	1683	5	32	0.18	0.1	1.1	0.2
I16272-4837	9	16h30m57.s90	−48d43m40.s47	2767	5	23	3.29	2.75	4.7	1.2
I16297-4757	3	16h33m29.s24	−48d03m26.s60	3472	3	27	1.24	0.85	0.9	0.3
I16297-4757	6	16h33m29.s82	−48d03m18.s20	2698	4	27	1.74	1.19	2.7	0.7
I16297-4757	8	16h33m29.s26	−48.03m39.s46	5888	2	27	2.71	1.86	0.4	0.2
I16297-4757	9	16h33m28.s97	−48d03m39.s60	5013	2	27	2.08	1.43	0.5	0.2
I16297-4757	10	16h33m29.s20	−48d03m37.s30	5801	1	27	2.2	1.51	0.3	0.2
I16304-4710	8	16h34m05.s05 s	−47d16m26.s87	7818	4	27	5.35	3.66	0.3	0.2
I16304-4710	10	16h34m04.s81	−47d16m24.s70	10316	3	27	4.53	3.11	0.1	0.1
I16313-4729	4	16h34m55.s59	−47d35m44.s52	3268	6	31	4.02	2.34	3.5	1.1
I16313-4729	7	16h34m55.s16	−47d35m41.s47	4587	3	31	3.97	2.3	1.2	0.5
I16313-4729	8	16h34m55.s82	−47d35m46.s88	2763	6	31	1.95	1.13	2.8	0.7
I16313-4729	9	16h34m55.s94	−47d35m54.s32	3241	4	31	4.12	2.39	3.7	1.1
I16344-4658[e]	**4**	**16h38m09.s90**	**−47d04m51.s68**	**7257**	**3**	**25**	**17.3**	**13.04**	**1.4**	**0.9**
I16362-4639	4	16h39m56.s62	−46d45m01.s89	1516	5	24	0.64	0.5	5.6	0.8
I16362-4639	5	16h39m58.s55	−46d45m01.s63	1764	4	24	0.52	0.41	2.9	0.5
I16362-4639	7	16h39m56.s55	−46d45m03.s07	1381	5	24	0.51	0.4	5.9	0.8
I16362-4639	8	16h39m58.s67	−46d45m00.s26	1597	4	24	0.44	0.35	3.3	0.5
I16362-4639	10	16h39m58.s03	−46d45m15.s10	1586	5	24	0.37	0.3	2.8	0.4
I16372-4545	9	16h40m53.s63	−45d50m54.s52	3591	3	26	1.79	1.29	1.2	0.4
I16385-4619	5	16h42m14.s73	−46d25m20.s68	6354	3	31	11.88	6.89	1.4	0.8
I16424-4531	13	16h46m05.s56	−45d36m40.s54	1420	6	24	0.52	0.41	5.5	0.7
I16445-4459	6	16h48m05.s58	−45d05m14.s50	6988	4	24	13.49	10.69	1.2	0.8
I16458-4512	12	16h49m30.s68	−45d18m02.s23	2387	5	21	4.67	4.39	10.4	2.3
I16489-4431	5	16h52m34.s71	−44d36m26.s79	1883	3	21	0.66	0.62	3.0	0.5
I17006-4215	8	17h04m13.s10	−42d19m54.s64	1637	3	27	0.44	0.3	3.0	0.5
I17204-3636	5	17h23m50.s76	−36d38m54.s57	2187	6	25	1.97	1.48	5.7	1.2
I17204-3636	6	17h23m50.s97	−36d38m55.s04	1879	5	25	1.32	1.0	6.0	1.1
I17204-3636	10	17h23m50.s71	−36d39m04.s83	2063	4	25	0.58	0.44	2.0	0.4
I17244-3536	3	17h27m48.s68	−35d39m21.s38	1437	4	29	1.22	0.77	12.4	1.7
I17244-3536	10	17h27m49.s81	−35d39m09.s70	1456	3	29	0.67	0.42	6.6	0.9
I17244-3536	12	17h27m48.s74	−35d39m05.s14	2072	5	29	0.78	0.49	2.7	0.5
I17244-3536	13	17h27m48.s20	−35d39m17.s07	2247	5	29	0.82	0.52	2.2	0.5
I17244-3536	14	17h27m49.s35	−35d39m11.s02	1322	4	29	0.49	0.31	6.4	0.8
I17258-3637	11	17h29m17.s20	−36d40m15 .s43	894	5	45	0.71	0.27	30.1	2.5
I17269-3312_1	3	17h30m15.s75	−33d14m50.s81	3837	3	22	4.22	3.74	2.3	0.8
I17269-3312_1	4	17h30m15.s76	−33d15m03.s13	3463	3	22	2.28	2.01	1.7	0.5
I17269-3312_1	5	17h30m15.s34	−33d14m46.s75	3340	1	22	2.82	2.49	2.3	0.7
I17269-3312_1	9	17h30m15.s57	−33d14m46.s20	2432	2	22	1.0	0.88	2.1	0.5
I17269-3312_2	5	17h30m14.s31	−33d14m14.s28	2746	2	22	0.95	0.84	1.4	0.4
I17278-3541	5	17h31m13.s22	−35d44m11.s60	657	4	25	0.2	0.15	21.4	1.3
I17278-3541	12	17h31m13.s46	−35d44m01.s58	1137	3	25	0.35	0.27	7.2	0.8
I17439-2845	9	17h47m08.s24	−28d46m11.s45	3980	3	30	12.2	7.37	5.9	2.2
I17545-2357	5	17h57m34.s47	−23d57m58.s20	2219	3	23	1.05	0.88	2.9	0.6
I18075-2040	2	18h10m34.s89	−20d39m11.s25	1971	3	23	0.3	0.25	1.2	0.2
I18075-2040	4	18h10m34.s47	−20d39m09.s24	2459	3	23	0.16	0.13	0.3	0.1
I18110-1854	9	18h14m00.s97	−18d53m18.s56	2311	2	28	1.22	0.8	3.0	0.6
I18116-1646	7	18h14m35.s75	−16d45m40.s22	2882	6	33	2.26	1.22	2.9	0.8
I18116-1646	10	18h14m35.s36	−16d45m34.s85	5050	6	33	1.66	0.89	0.4	0.2
I18139-1842	9	18h16m50.s89	−18d41m28.s39	1987	5	40	1.06	0.46	4.1	0.8
I18223-1243	9	18h25m10.s76	−12d42m20.s10	3059	6	23	1.25	1.05	1.3	0.4
I18290-0924	3	18h31m42.s68	−9d22m27.s48	2666	5	22	6.0	5.31	9.6	2.4

Table 4
(Continued)

Source	Core	RA (IRCS) (h:m:s)	Decl. (IRCS) (d:m:s)	R (au)	N_{line}[a]	Temp.[b] (K)	$Mass_{upper}$[c] ($M_\odot$)	$Mass_{lower}$[c] ($M_\odot$)	$n_{H_2(20\,K)}$[d] ($\times 10^6$ cm^{-3})	$\Sigma_{(20\,K)}$[d] (g cm^{-2})
(1)	(2)	(3)	(4)	(5)	(6)	(7)	(8)	(9)	(10)	(11)
I18290-0924	5	$18^h31^m43\overset{s}{.}07$	$-9^d22^m23\overset{s}{.}06$	3090	5	22	1.91	1.69	2.0	0.6
I18290-0924	6	$18^h31^m43\overset{s}{.}72$	$-9^d22^m12\overset{s}{.}20$	3387	4	22	1.59	1.41	1.2	0.4
I18290-0924	7	$18^h31^m43\overset{s}{.}55$	$-9^d22^m30\overset{s}{.}92$	2656	3	22	0.97	0.86	1.6	0.4
I18290-0924	9	$18^h31^m43\overset{s}{.}26$	$-9^d22^m33\overset{s}{.}82$	3503	4	22	0.92	0.82	0.6	0.2
I18290-0924	11	$18^h31^m43\overset{s}{.}11$	$-9^d22^m13\overset{s}{.}70$	4469	1	22	1.01	0.9	0.3	0.1
I18290-0924	12	$18^h31^m43\overset{s}{.}50$	$-9^d22^m29\overset{s}{.}54$	2683	4	22	0.68	0.6	1.1	0.3
I18308-0503	2	$18^h33^m30\overset{s}{.}45$	$-5^d00^m55\overset{s}{.}16$	2546	5	31	2.24	1.3	4.1	1.0
I18308-0503	4	$18^h33^m29\overset{s}{.}22$	$-5^d01^m00\overset{s}{.}13$	3230	1	31	1.23	0.72	1.1	0.3
I18308-0503	7	$18^h33^m29\overset{s}{.}38$	$-5^d00^m59\overset{s}{.}50$	2685	4	31	0.81	0.47	1.3	0.3
I18308-0503	8	$18^h33^m29\overset{s}{.}59$	$-5^d00^m57\overset{s}{.}60$	1953	3	31	0.37	0.21	1.5	0.3
I18314-0720	16	$18^h34^m08\overset{s}{.}48$	$-7^d17^m50\overset{s}{.}41$	3488	3	30	1.77	1.07	1.3	0.4
I18317-0513	8	$18^h34^m26\overset{s}{.}36$	$-5^d10^m56\overset{s}{.}10$	2783	2	31	1.91	1.11	2.7	0.7
I18317-0513	14	$18^h34^m25\overset{s}{.}49$	$-5^d11^m00\overset{s}{.}10$	1518	3	31	0.38	0.22	3.3	0.5
I18317-0757	5	$18^h34^m25\overset{s}{.}29$	$-7^d54^m44\overset{s}{.}68$	2386	2	30	2.69	1.62	6.0	1.3
I18317-0757	12	$18^h34^m25\overset{s}{.}36$	$-7^d54^m41\overset{s}{.}40$	5002	1	30	5.7	3.44	1.4	0.6
I18411-0338	8	$18^h43^m46\overset{s}{.}23$	$-3^d35^m24\overset{s}{.}21$	5616	5	27	4.38	3.0	0.7	0.4
I18440-0148	2	$18^h46^m36\overset{s}{.}14$	$-1^d45^m16\overset{s}{.}98$	9251	3	33	4.8	2.59	0.2	0.2
I18440-0148	4	$18^h46^m36\overset{s}{.}91$	$-1^d45^m28\overset{s}{.}32$	5407	4	33	1.94	1.05	0.4	0.2
I18440-0148	6	$18^h46^m36\overset{s}{.}33$	$-1^d45^m19\overset{s}{.}13$	9054	4	33	3.19	1.72	0.1	0.1
I18440-0148	7	$18^h46^m37\overset{s}{.}17$	$-1^d45^m17\overset{s}{.}23$	7086	3	33	2.47	1.33	0.2	0.1
I18445-0222	3	$18^h47^m09\overset{s}{.}50$	$-2^d18^m48\overset{s}{.}17$	6251	3	27	9.35	6.41	1.2	0.7
I18445-0222	6	$18^h47^m09\overset{s}{.}62$	$-2^d18^m42\overset{s}{.}45$	4642	5	27	3.21	2.2	1.0	0.4
I18445-0222	7	$18^h47^m09\ \overset{s}{.}73$	$-2^d18^m42\overset{s}{.}22$	4590	6	27	3.06	2.1	1.0	0.4
I18445-0222	9	$18^h47^m10\overset{s}{.}72$	$-2^d18^m46\overset{s}{.}60$	3262	3	27	1.39	0.95	1.2	0.4
I18461-0113	5	$18^h48^m43\overset{s}{.}03$	$-1^d10^m03\overset{s}{.}78$	3170	1	27	5.23	3.59	5.0	1.5
I18507+0121	2	$18^h53^m18\overset{s}{.}28$	$1^d25^m13\overset{s}{.}68$	2651	3	22	7.0	6.19	11.4	2.8
I18507+0121	7	$18^h53^m18\overset{s}{.}75$	$1^d25^m26\overset{s}{.}47$	2455	3	22	3.13	2.77	6.4	1.5
I18530+0215	7	$18^h55^m32\overset{s}{.}97$	$2^d19^m02\overset{s}{.}74$	4296	5	26	7.45	5.35	2.8	1.1
I19097+0847	8	$19^h12^m09\overset{s}{.}62$	$8^d52^m06\overset{s}{.}24$	6281	4	23	5.74	4.8	0.7	0.4
I19097+0847	11	$19^h12^m09\overset{s}{.}60$	$8^d52^m13\overset{s}{.}00$	3307	5	23	3.03	2.53	2.5	0.8

Notes.
[a] The number of molecular lines detected for each core.
[b] The dust temperature of the parental clump.
[c] The upper and lower masses were calculated corresponding to the assumed 20 K typical for candidate starless cores in the IR-bright environment and the average temperature of the parental clump, respectively. Note that since there are two cores (i.e., in I13295-6152 clumps) whose parental clump has an average temperature slightly lower than 20 K, the upper and lower mass estimates were switched manually.
[d] The number and the surface density of each core are estimated for the 20 K temperature.
[e] Candidate high-mass starless core.

(This table is available in machine-readable form in the online article.)

Table 5
Derived Parameters for Candidate Warm and Evolved Cores

Source	Core	R.A. (IRCS) (h:m:s)	Decl. (IRCS) (d:m:s)	R (au)	$N_{\rm line}$[a]	Temp.[b] (K)	Mass ($M_\odot$)	$n_{\rm H_2}$ ($\times 10^5$ cm^{-3})	Σ (g cm^{-2})	Evol.[c]
(1)	(2)	(3)	(4)	(5)	(6)	(7)	(8)	(9)	(10)	(11)
I08303-4303	1	$8^h32^m08\overset{s}{.}64$	$-43^d13^m45\overset{s}{.}65$	1180	48	100.0	2.54	468.92	5.17	HMC
I08303-4303	2	$8^h32^m09\overset{s}{.}05$	$-43^d13^m43\overset{s}{.}33$	949	11	30.0	2.41	854.36	7.57	WC
I08303-4303	3	$8^h32^m08\overset{s}{.}46$	$-43^d13^m49\overset{s}{.}13$	1374	18	100.0	1.0	116.99	1.5	HMC
I08303-4303	4	$8^h32^m08\overset{s}{.}46$	$-43^d13^m47\overset{s}{.}22$	1157	16	100.0	0.54	105.47	1.14	HMC
I08303-4303	5	$8^h32^m08\overset{s}{.}90$	$-43^d13^m52\overset{s}{.}12$	1094	10	30.0	0.45	103.52	1.06	WC
I08303-4303	6	$8^h32^m08\overset{s}{.}88$	$-43^d13^m42\overset{s}{.}05$	2006	11	30.0	0.55	20.63	0.39	WC
I08448-4343	1	$8^h46^m32\overset{s}{.}31$	$-43^d54^m36\overset{s}{.}85$	478	14	30.0	1.18	3278.14	14.64	WC
I08448-4343	2	$8^h46^m33\overset{s}{.}39$	$-43^d54^m37\overset{s}{.}28$	583	15	30.0	0.93	1427.41	7.77	WC
I08448-4343	3	$8^h46^m34\overset{s}{.}84$	$-43^d54^m30\overset{s}{.}10$	401	8	100.0	0.08	377.86	1.42	UCHII-*l*
I08448-4343	4	$8^h46^m34\overset{s}{.}32$	$-43^d54^m39\overset{s}{.}51$	462	7	30.0	0.19	586.74	2.53	WC
I08448-4343	5	$8^h46^m31\overset{s}{.}17$	$-43^d54^m36\overset{s}{.}47$	451	5	30.0	0.2	663.82	2.8	WC
I08448-4343	6	$8^h46^m34\overset{s}{.}94$	$-43^d54^m23\overset{s}{.}65$	534	10	30.0	0.25	488.04	2.43	WC
I08448-4343	7	$8^h46^m34\overset{s}{.}63$	$-43^d54^m32\overset{s}{.}50$	711	9	30.0	0.33	275.41	1.83	WC
I08448-4343	8	$8^h46^m31\overset{s}{.}79$	$-43^d54^m36\overset{s}{.}02$	470	9	30.0	0.16	454.3	1.99	WC
I08448-4343	10	$8^h46^m33\overset{s}{.}33$	$-43^d54^m38\overset{s}{.}56$	504	10	30.0	0.19	458.13	2.16	WC
I08448-4343	11	$8^h46^m33\overset{s}{.}30$	$-43^d54^m34\overset{s}{.}67$	439	10	30.0	0.17	604.03	2.48	WC
I08448-4343	12	$8^h46^m33\overset{s}{.}65$	$-43^d54^m34\overset{s}{.}66$	461	11	30.0	0.15	473.6	2.04	WC
I08448-4343	13	$8^h46^m35\overset{s}{.}12$	$-43^d54^m24\overset{s}{.}25$	630	13	30.0	0.27	331.56	1.95	WC
I08448-4343	14	$8^h46^m34\overset{s}{.}90$	$-43^d54^m26\overset{s}{.}72$	428	11	30.0	0.11	438.45	1.75	WC
I08448-4343	15	$8^h46^m33\overset{s}{.}74$	$-43^d54^m34\overset{s}{.}22$	481	10	30.0	0.13	360.88	1.62	WC
I08448-4343	16	$8^h46^m32\overset{s}{.}22$	$-43^d54^m40\overset{s}{.}99$	488	6	30.0	0.1	263.18	1.2	WC
I08448-4343	17	$8^h46^m32\overset{s}{.}96$	$-43^d54^m34\overset{s}{.}82$	437	9	30.0	0.1	370.67	1.51	WC
I08448-4343	18	$8^h46^m33\overset{s}{.}57$	$-43^d54^m34\overset{s}{.}90$	376	9	30.0	0.09	484.54	1.7	WC
I08448-4343	19	$8^h46^m32\overset{s}{.}13$	$-43^d54^m41\overset{s}{.}71$	382	6	30.0	0.05	297.98	1.06	WC
I08448-4343	21	$8^h46^m32\overset{s}{.}50$	$-43^d54^m37\overset{s}{.}09$	517	11	30.0	0.09	194.24	0.94	WC
I08448-4343	22	$8^h46^m34\overset{s}{.}74$	$-43^d54^m20\overset{s}{.}61$	1013	7	30.0	0.15	44.31	0.42	WC
I08448-4343	23	$8^h46^m32\overset{s}{.}66$	$-43^d54^m35\overset{s}{.}87$	1583	8	30.0	0.69	52.48	0.78	WC
I08448-4343	24	$8^h46^m33\overset{s}{.}37$	$-43^d54^m28\overset{s}{.}29$	1201	9	30.0	0.09	15.09	0.17	WC
I08448-4343	25	$8^h46^m34\overset{s}{.}83$	$-43^d54m32\overset{s}{.}67$	670	9	30.0	0.07	69.81	0.44	WC
I08448-4343	26	$8^h46^m33\overset{s}{.}76$	$-43^d54^m37\overset{s}{.}19$	945	7	30.0	0.07	25.4	0.22	WC

Notes.
[a] The number of molecular lines detected for each core.
[b] The dust temperature for the warm and evolved core candidates was assumed to be 30 K and 100 K, respectively.
[c] The evolutionary stage of each core: "WC," "HMC," "UCHII-*h*," and UCHII-*l*, corresponding to warm core, hot molecular core, UCHII core with a high line richness ($N_{\rm line} \geqslant 15$), and UCHII core with a low line richness ($6 < N_{\rm line} < 15$) candidates, respectively.

(This table is available in its entirety in machine-readable form in the online article.)

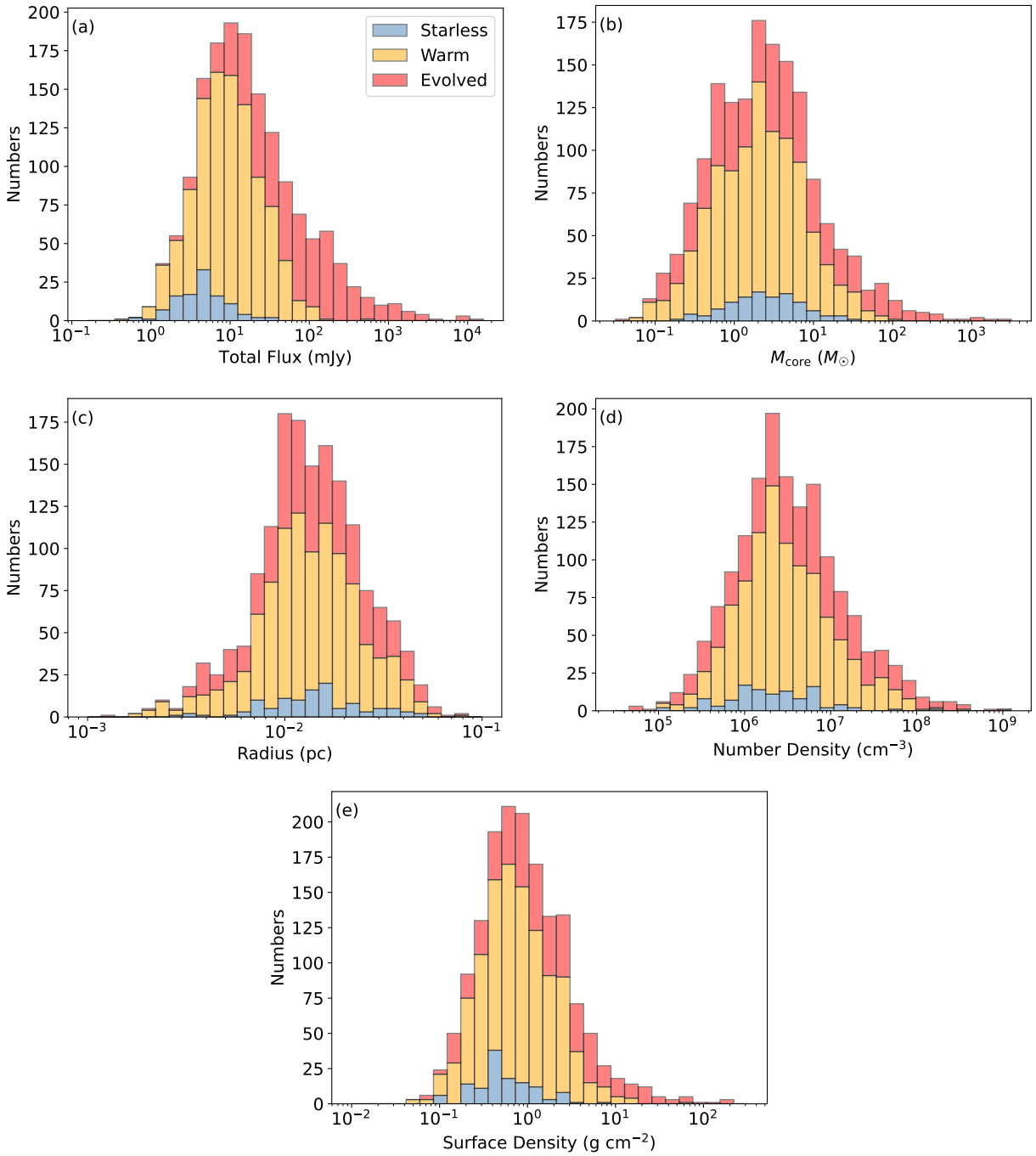

Figure 10. Distribution of physical parameters of the QUARKS TM2+ACA dense cores against evolutionary stage. Panels (a)–(e) present the parameter of total flux, mass, radius, number density, and surface density, respectively.

Appendix B
Impact of Various Clump Distances

Figure 11 shows the distribution of median linear core separation within each clump as a function of source distance, revealing a strong positive correlation that corresponds to a Spearman's coefficient of $\rho_s \sim 0.9$ and a p-value of $\ll 0.01$. Figure 12 displays the relationships between source distance and core mass (panel (a)) and the surface density of core count within each clump (panel (b)). Core mass shows a strong positive correlation with distance ($\rho_s \sim 0.8$ and $p \ll 0.01$), while core count surface density shows a strong negative correlation ($\rho_s \sim -0.9$ and $p \ll 0.01$). Figure 13(a) plots the thermal Jeans length of the clump against source distance, showing a positive correlation ($\rho_s \sim 0.6$ and $p \ll 0.01$). Figure 13(b) presents the ratio $\lambda_{\rm obs}/\lambda_{\rm J}$ as a function of the source distance, indicating a weak or no correlation ($\rho_s \sim 0.4$ and $p \ll 0.01$) between these two quantities.

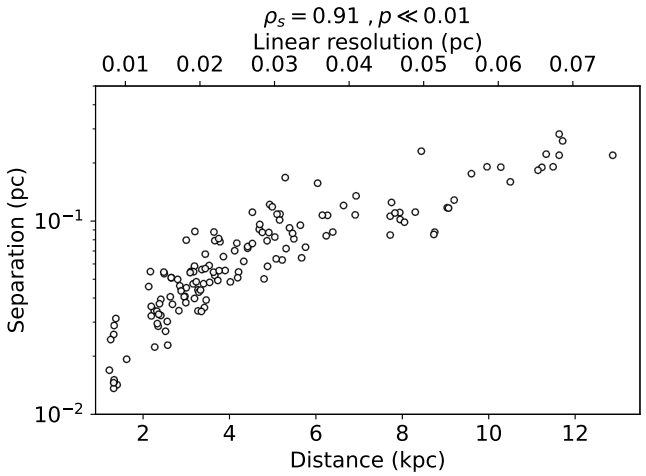

Figure 11. Distribution of the median linear core separation within each clump against the source distance. The Spearman's rank correlation coefficient ($\rho_s = 0.9$) and the probability value ($p \ll 0.01$) of the distribution are shown on the top. The upper x-axis also displays the spatial resolution at the corresponding distance.

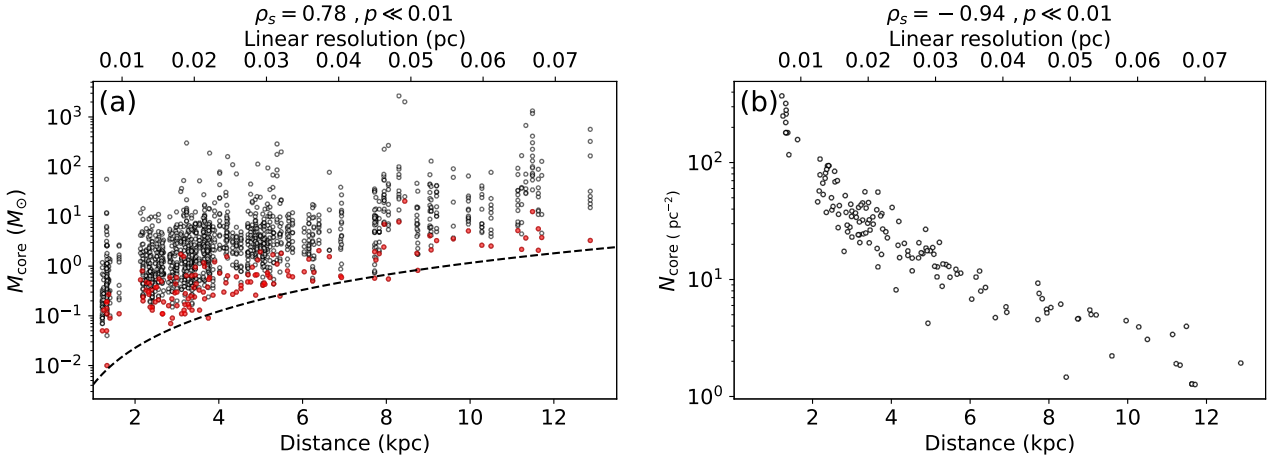

Figure 12. (a) Distribution of the core mass against the source distance. The red circle symbols display the minimum core mass detected within each clump. The black dashed curve fits the lower envelope of the minimum core masses as a function of the distance. (b) Distribution of the surface density of the core count within each clump against the source distance. The top of both panels shows the Spearman's rank correlation coefficient (ρ_s) and the probability value (p) of the distribution. The upper x-axis of both panels also displays the spatial resolution at the corresponding distance.

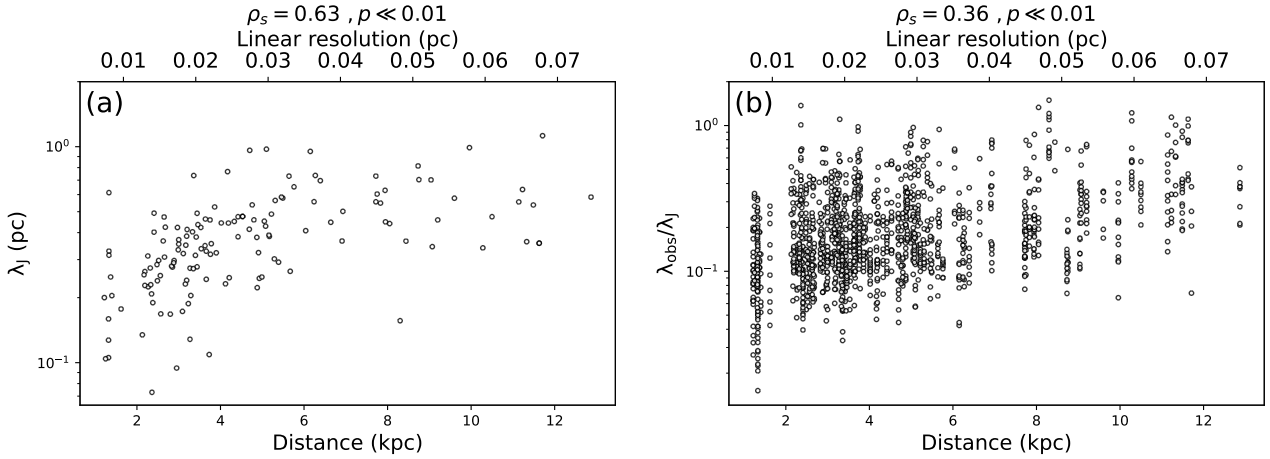

Figure 13. (a) Thermal Jeans length vs. protocluster clumps distance. (b) Ratio of core separation to thermal Jeans length vs. protocluster clumps distance.

Appendix C
Additional Information for Candidate Starless Cores

We provide additional information here for two candidate high-mass starless cores. The molecular line emission of each high-mass starless core candidate is shown in Figure 14, and the CO molecular outflow maps overlaid on the QUARKS 1.3 mm continuum image are presented in Figure 15. In Figure 16, we present a comparison between ATOMS "unknown" sources (H.-L. Liu et al. 2021) and QUARKS TM2+ACA starless cores for the mass and size parameters. Note that only 26 ATOMS "unknown" sources that are related to candidate starless cores from the QUARKS survey are depicted in this figure. We find that the ATOMS "unknown" sources generally exhibit about 1 dex larger sizes and masses. This suggests that the lower angular resolution at 3 mm is capable of detecting more extended envelope emissions, while the higher angular resolution at 1.3 mm is better suited to trace the kernel of the cores.

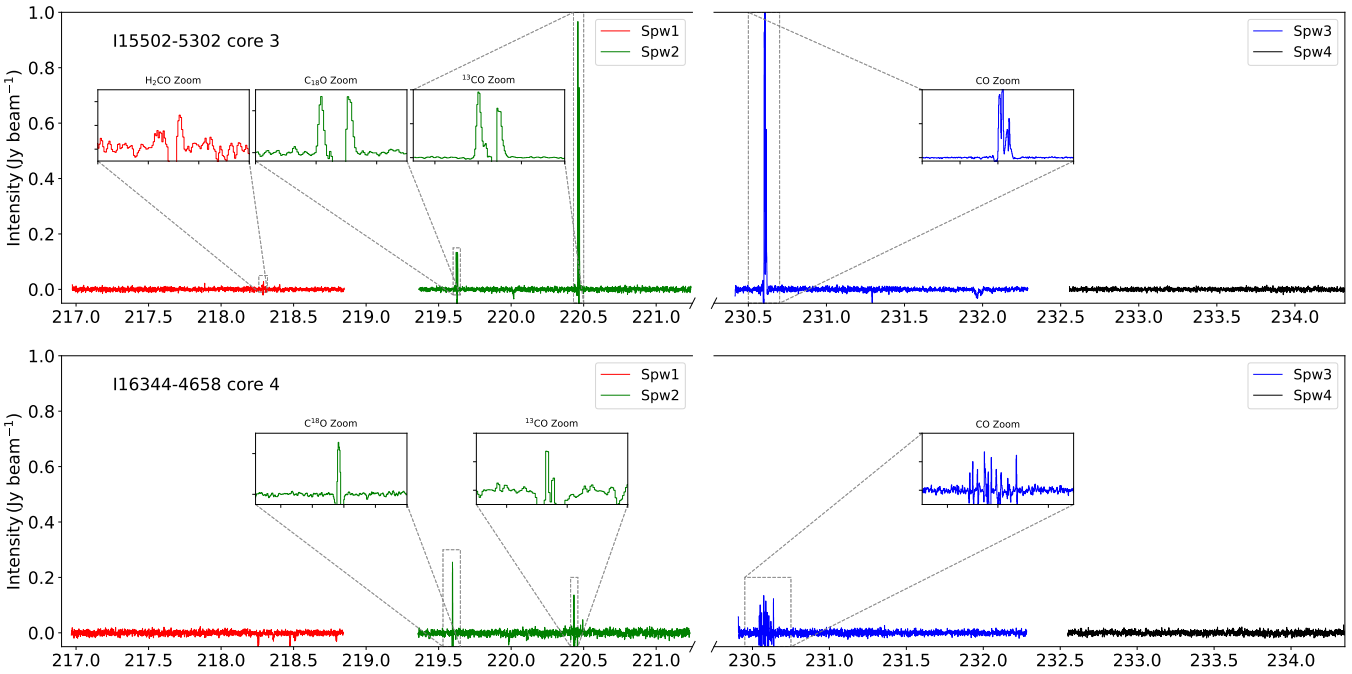

Figure 14. Core-averaged spectra of two high-mass starless core candidates from four QUARKS SPWs. Note that the zoom-in of the CO line spectrum in the bottom panel presents many artificial absorption dips caused by missing flux of extended gas structures, which, however, do not affect our classification of candidate starless cores. These artifacts can be addressed in the future by combing our QUARKS and single-dish observations.

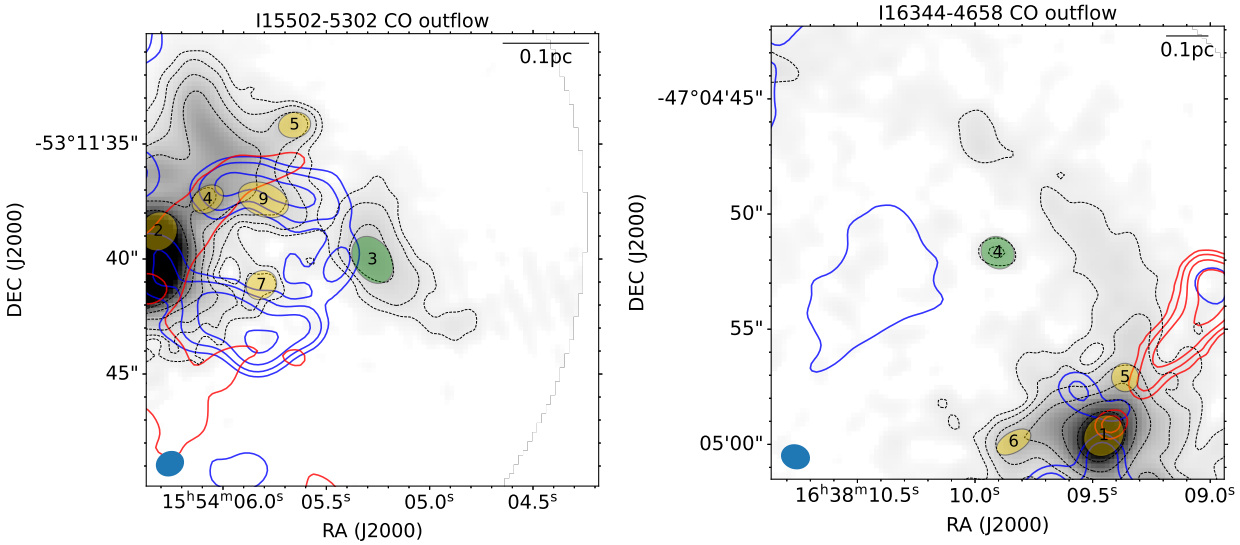

Figure 15. CO molecular outflow overlaid on the 1.3 mm dust continuum map of two protocluster clumps containing high-mass starless core candidates. The velocity offset is set around $V_{\rm LSR}$ ± 10–30 km s^{-1}. The red and blue contours start at 3 rms (∼0.2 mJy beam^{-1} km s^{-1}) and follow as [6, 12, 24, 48] rms. High-mass starless core candidates in this study are shown as green circles. ALMA-QUARKS TM2+ACA 1.3 mm dust continuum contour levels are [3, 6, 12, 24, 48] rms, with an rms of ∼0.6 mJy beam^{-1}.

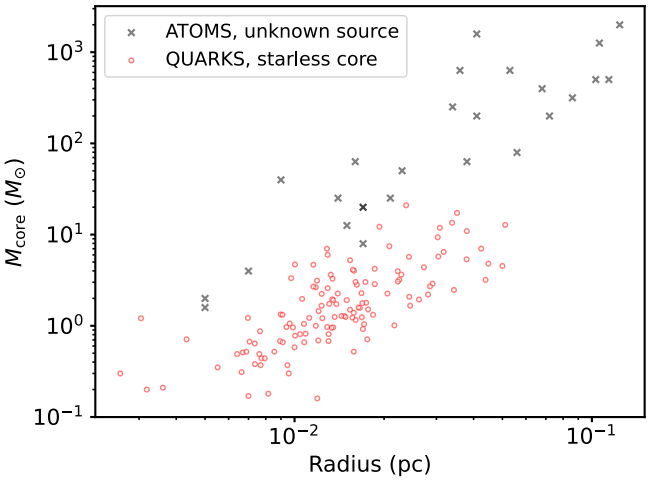

Figure 16. Mass–radius relation between ATOMS "unknown" sources and candidate starless cores of the QUARKS TM2+ACA catalog.

ORCID iDs

Dongting Yang https://orcid.org/0009-0004-6159-5375
Hong-Li Liu https://orcid.org/0000-0003-3343-9645
Tie Liu https://orcid.org/0000-0002-5286-2564
Xunchuan Liu https://orcid.org/0000-0001-8315-4248
Fengwei Xu https://orcid.org/0000-0001-5950-1932
Sheng-Li Qin https://orcid.org/0000-0003-2302-0613
Anandmayee Tej https://orcid.org/0000-0001-5917-5751
Xiaofeng Mai https://orcid.org/0000-0001-7573-0145
Wenyu Jiao https://orcid.org/0000-0001-9822-7817
Sami Dib https://orcid.org/0000-0002-8697-9808
Amelia M. Stutz https://orcid.org/0000-0003-2300-8200
Aina Palau https://orcid.org/0000-0002-9569-9234
Patricio Sanhueza https://orcid.org/0000-0002-7125-7685
Annie Zavagno https://orcid.org/0000-0001-9509-7316
A. Y. Yang https://orcid.org/0000-0003-4546-2623
Xindi Tang https://orcid.org/0000-0002-4154-4309
Mengyao Tang https://orcid.org/0000-0001-9160-2944
Pablo García https://orcid.org/0000-0002-8586-6721
Tianwei Zhang https://orcid.org/0000-0002-1466-3484
Anindya Saha https://orcid.org/0000-0002-9793-3039
Shanghuo Li https://orcid.org/0000-0003-1275-5251
Paul F. Goldsmith https://orcid.org/0000-0002-6622-8396
Leonardo Bronfman https://orcid.org/0000-0002-9574-8454
Chang Won Lee https://orcid.org/0000-0002-3179-6334
Kotomi Taniguchi https://orcid.org/0000-0003-4402-6475
Swagat Ranjan Das https://orcid.org/0000-0002-3658-0516
Prasanta Gorai https://orcid.org/0000-0003-1602-6849
Ariful Hoque https://orcid.org/0009-0003-6633-525X
Li Chen https://orcid.org/0009-0009-8154-4205
L. Viktor Tóth https://orcid.org/0000-0002-5310-4212
Tapas Baug https://orcid.org/0000-0003-0295-6586
Xianjin Shen https://orcid.org/0009-0004-3244-3508
Jiahang Zou https://orcid.org/0009-0000-9090-9960
Ankan Das https://orcid.org/0000-0003-4615-602X
L. K. Dewangan https://orcid.org/0000-0001-6725-0483
Jihye Hwang https://orcid.org/0000-0001-7866-2686
James O. Chibueze https://orcid.org/0000-0002-9875-7436

References

Avison, A., Fuller, G. A., Frimpong, N. A., et al. 2023, MNRAS, 526, 2278
Barnes, A. T., Henshaw, J. D., Fontani, F., et al. 2021, MNRAS, 503, 4601
Barnes, A. T., Liu, J., Zhang, Q., et al. 2023, A&A, 675, A53
Barrow, J. D., Bhavsar, S. P., & Sonoda, D. H. 1985, MNRAS, 216, 17
Benedettini, M., Pezzuto, S., Schisano, E., et al. 2018, A&A, 619, A52
Bertoldi, F., & McKee, C. F. 1992, ApJ, 395, 140
Beuther, H., Kuiper, R., & Tafalla, M. 2025, ARA&A, 63, 1
Beuther, H., Semenov, D., Henning, T., & Linz, H. 2008, ApJL, 675, L33
Beuther, H., Mottram, J. C., Ahmadi, A., et al. 2018, A&A, 617, A100
Bonnell, I. A., Bate, M. R., Clarke, C. J., & Pringle, J. E. 2001, MNRAS, 323, 785
Bronfman, L., Nyman, L. A., & May, J. 1996, A&AS, 115, 81
CASA Team, Bean, B., Bhatnagar, S., et al. 2022, PASP, 134, 114501
Chen, L., Qin, S.-L., Liu, T., et al. 2025, A&A, 694, A166
Codella, C., Ceccarelli, C., Lefloch, B., et al. 2012, ApJL, 757, L9
Coletta, A., Molinari, S., Schisano, E., et al. 2025, A&A, 696, A151
Commerçon, B., Hennebelle, P., & Henning, T. 2011, ApJL, 742, L9
Das, S. R., Merello, M., Bronfman, L., et al. 2024, MNRAS, 534, 3832
Dell'Ova, P., Motte, F., Gusdorf, A., et al. 2024, A&A, 687, A217
Dewangan, L. K., Bhadari, N. K., Maity, A. K., et al. 2024, MNRAS, 527, 5895
Dewangan, L. K., Bhadari, N. K., Men'shchikov, A., et al. 2023, ApJ, 946, 22
Dib, S., Bell, E., & Burkert, A. 2006, ApJ, 638, 797
Dib, S., & Henning, T. 2019, A&A, 629, A135
Dib, S., Kim, J., Vázquez-Semadeni, E., Burkert, A., & Shadmehri, M. 2007, ApJ, 661, 262
Dobbs, C. L., Krumholz, M. R., Ballesteros-Paredes, J., et al. 2014, in Protostars and Planets VI, ed. H. Beuther et al. (Tucson, AZ: Univ. Arizona Press), 3
Faúndez, S., Bronfman, L., Garay, G., et al. 2004, A&A, 426, 97
Fontani, F., Commerçon, B., Giannetti, A., et al. 2016, A&A, 593, L14
Ginsburg, A., Anderson, L. D., Dicker, S., et al. 2020, ApJS, 248, 24
Girichidis, P., Federrath, C., Banerjee, R., & Klessen, R. S. 2011, MNRAS, 413, 2741
Hennebelle, P., Lebreuilly, U., Colman, T., et al. 2022, A&A, 668, A147
Herbst, E., & van Dishoeck, E. F. 2009, ARA&A, 47, 427
Ishihara, K., Sanhueza, P., Nakamura, F., et al. 2024, ApJ, 974, 95
Jiao, W., Wang, K., Pillai, T. G. S., et al. 2023, ApJ, 945, 81
Kauffmann, J., Bertoldi, F., Bourke, T. L., Evans, N. J., II, & Lee, C. W. 2008, A&A, 487, 993
Klos, K. S., Bonnell, I. A., & Smith, R. J. 2025, MNRAS, 539, 2307
Kou, Z., Li, X., Qin, S.-L., et al. 2025, MNRAS, 538, 2579
Li, S., Zhang, Q., Pillai, T., et al. 2019, ApJ, 886, 130
Li, Z.-Y., Liu, X., Liu, T., et al. 2025, A&A, 697, A190
Liu, H.-L., Liu, T., Evans, N. J., II, et al. 2021, MNRAS, 505, 2801
Liu, H.-L., Tej, A., Liu, T., et al. 2022a, MNRAS, 510, 5009
Liu, H.-L., Tej, A., Liu, T., et al. 2023, MNRAS, 522, 3719
Liu, R., Liu, T., Chen, G., et al. 2022b, MNRAS, 511, 3618
Liu, T., Lacy, J., Li, P. S., et al. 2017, ApJ, 849, 25
Liu, T., Evans, N. J., Kim, K.-T., et al. 2020, MNRAS, 496, 2790
Liu, X., Liu, T., Zhu, L., et al. 2024, RAA, 24, 025009
Louvet, F., Sanhueza, P., Stutz, A., et al. 2024, A&A, 690, A33
Lu, X., Cheng, Y., Ginsburg, A., et al. 2020, ApJL, 894, L14
Luo, A.-X., Liu, H.-L., Li, G.-X., Pan, S., & Yang, D.-T. 2024a, RAA, 24, 065003
Luo, A.-X., Liu, H.-L., Qin, S.-L., Yang, D.-t., & Pan, S. 2024b, AJ, 167, 228
Mai, X., Liu, T., Liu, X., et al. 2024, ApJL, 961, L35
McKee, C. F., & Tan, J. C. 2003, ApJ, 585, 850
Men'shchikov, A. 2021, A&A, 649, A89
Morii, K., Sanhueza, P., Nakamura, F., et al. 2023, ApJ, 950, 148
Morii, K., Sanhueza, P., Zhang, Q., et al. 2024, ApJ, 966, 171
Motte, F., Bontemps, S., & Louvet, F. 2018, ARA&A, 56, 41
Motte, F., Bontemps, S., Csengeri, T., et al. 2022, A&A, 662, A8
Müller, H. S. P., Thorwirth, S., Roth, D. A., & Winnewisser, G. 2001, A&A, 370, L49
Nony, T., Louvet, F., Motte, F., et al. 2018, A&A, 618, L5
Nony, T., Galván-Madrid, R., Motte, F., et al. 2023, A&A, 674, A75
Ossenkopf, V., & Henning, T. 1994, A&A, 291, 943
Padoan, P., Pan, L., Juvela, M., Haugbølle, T., & Nordlund, Å. 2020, ApJ, 900, 82
Palau, A., Estalella, R., Girart, J. M., et al. 2014, ApJ, 785, 42
Palau, A., Ballesteros-Paredes, J., Vázquez-Semadeni, E., et al. 2015, MNRAS, 453, 3785
Palau, A., Zapata, L. A., Román-Zúñiga, C. G., et al. 2018, ApJ, 855, 24
Palau, A., Zhang, Q., Girart, J. M., et al. 2021, ApJ, 912, 159
Pan, S., Liu, H.-L., & Qin, S.-L. 2024, ApJ, 960, 76
Peng, Y., Liu, T., Qin, S.-L., et al. 2022, MNRAS, 512, 4419
Peretto, N., Fuller, G. A., Duarte-Cabral, A., et al. 2013, A&A, 555, A112

Peters, T., Banerjee, R., Klessen, R. S., & Mac Low, M.-M. 2011, ApJ, 729, 72
Pillai, T., Kauffmann, J., Wyrowski, F., et al. 2011, A&A, 530, A118
Pouteau, Y., Motte, F., Nony, T., et al. 2022, A&A, 664, A26
Qin, S.-L., Schilke, P., Wu, J., et al. 2015, ApJ, 803, 39
Qin, S.-L., Liu, T., Liu, X., et al. 2022, MNRAS, 511, 3463
Rau, U., & Cornwell, T. J. 2011, A&A, 532, A71
Requena-Torres, M. A., Martín-Pintado, J., Rodríguez-Franco, A., et al. 2006, A&A, 455, 971
Richards, A. M. S., Moravec, E., Etoka, S., et al. 2022, arXiv:2207.05591
Saha, A., Tej, A., Liu, H.-L., et al. 2022, MNRAS, 516, 1983
Saha, P., Sanhueza, P., Padovani, M., et al. 2024, ApJL, 972, L6
Sánchez-Monge, Á., Palau, A., Fontani, F., et al. 2013, MNRAS, 432, 3288
Sanhueza, P., Jackson, J. M., Foster, J. B., et al. 2013, ApJ, 773, 123
Sanhueza, P., Jackson, J. M., Zhang, Q., et al. 2017, ApJ, 841, 97
Sanhueza, P., Contreras, Y., Wu, B., et al. 2019, ApJ, 886, 102
Sanhueza, P., Liu, J., Morii, K., et al. 2025, ApJ, 980, 87
Shen, X., Liu, H.-L., Ren, Z., et al. 2024, ApJ, 974, 239
Svoboda, B. E., Shirley, Y. L., Traficante, A., et al. 2019, ApJ, 886, 36
Tang, M., Palau, A., Zapata, L. A., & Qin, S.-L. 2022, A&A, 657, A30
Taniguchi, K., Sanhueza, P., Olguin, F. A., et al. 2023, ApJ, 950, 57
Teixeira, P. S., Takahashi, S., Zapata, L. A., & Ho, P. T. P. 2016, A&A, 587, A47
Traficante, A., Jones, B. M., Avison, A., et al. 2023, MNRAS, 520, 2306
Urquhart, J. S., Wells, M. R. A., Pillai, T., et al. 2022, MNRAS, 510, 3389
Valeille-Manet, M., Bontemps, S., Csengeri, T., et al. 2025, A&A, 696, A11
Vázquez-Semadeni, E., Palau, A., Ballesteros-Paredes, J., Gómez, G. C., & Zamora-Avilés, M. 2019, MNRAS, 490, 3061
Wang, K., Zhang, Q., Testi, L., et al. 2014, MNRAS, 439, 3275
Wang, K., Chen, Z. B., Si, R., et al. 2016, ApJS, 226, 14
Xu, F., Wang, K., Liu, T., et al. 2024a, ApJS, 270, 9
Xu, F., Wang, K., Liu, T., et al. 2024b, RAA, 24, 065011
Xu, F., Lu, X., Wang, K., et al. 2025, A&A, 697, A164
Xu, F.-W., Wang, K., Liu, T., et al. 2023, MNRAS, 520, 3259
Yang, A. Y., Thompson, M. A., Urquhart, J. S., & Tian, W. W. 2018, ApJS, 235, 3
Yang, A. Y., Urquhart, J. S., Wyrowski, F., et al. 2022, A&A, 658, A160
Yang, D., Liu, H.-L., Tej, A., et al. 2023, ApJ, 953, 40
Yang, D., Liu, H.-L., Liu, T., et al. 2024, ApJ, 976, 241
Zhang, C., Evans, N. J., Liu, T., et al. 2022, MNRAS, 510, 4998
Zhang, C., Zhu, F.-Y., Liu, T., et al. 2023a, MNRAS, 520, 3245
Zhang, C., Liu, T., Ren, Z. Y., et al. 2024, MNRAS, 533, 4234
Zhang, Q., & Wang, K. 2011, ApJ, 733, 26
Zhang, Q., Wang, K., Lu, X., & Jiménez-Serra, I. 2015, ApJ, 804, 141
Zhang, Q., Wang, Y., Pillai, T., & Rathborne, J. 2009, ApJ, 696, 268
Zhang, S., Zavagno, A., López-Sepulcre, A., et al. 2021, A&A, 646, A25
Zhang, S., Wang, K., Liu, T., et al. 2023b, MNRAS, 520, 322
Zhou, J.-W., Liu, T., Li, J.-Z., et al. 2021, MNRAS, 508, 4639
Zhou, J.-W., Liu, T., Evans, N. J., et al. 2022, MNRAS, 514, 6038
Zinnecker, H., & Yorke, H. W. 2007, ARA&A, 45, 481